Energy Harvesting in the Course of Acid Solution Neutralization

Bianca Tainá Ferreira[1], Daniel Rueda-García[2], Pedro Gómez-Romero[2], and

Fritz Huguenin[1,*]

1- Departamento de Química, Faculdade de Filosofia, Ciências e Letras de Ribeirão Preto – Universidade de São Paulo, 14040-901 Ribeirão Preto (SP), Brazil

2 - Catalan Institute of Nanoscience and Nanotechnology (ICN2), and The Barcelona Institute of Science and Technology (CSIC-BIST), Campus UAB, Bellaterra, 08193 Barcelona, Spain

*e-mail: fritz@ffclrp.usp.br

ABSTRACT

This work investigates electrodes consisting of phosphomolybdic acid/reduced graphene oxide (PMo_{12}/RGO) and copper hexacyanoferrate (CuHCF) for proton adsorption/desorption and alkali metal ion intercalation/deintercalation, respectively. These electrodes can be used to harvest the energy resulting from the difference in ion concentrations during acid solution neutralization. $H_3PMo_{12}O_{40}$ clusters were uniformly anchored on RGO sheets to ensure large electrode surface area and to facilitate proton access to the polyoxometalate electroactive sites. On the other hand, compared to iron ions in Prussian Blue, copper ions in the hexacyanometalate structure provided higher potassium ion intercalation/deintercalation rate. The experiments were performed in the time and frequency domains, and thermodynamic and kinetic models were proposed to improve our understanding of how the electrochemical system behaves with respect to energy harvesting. The reactions presented low energy dissipation due to low charge transfer resistance and diffusion impedance. The predicted energy harvested by the electrochemical full cell was 13.5 and 10.7 kJ per mol of adsorbed proton at 0.1 and 1.0 mA cm^{-2} in acidic (pH = 2) and slightly acidic (pH = 6) media, respectively, which included acetate buffer and the feedback of the saline solution resulting from neutralization. The electrodes used here provided increased energy harvesting and power density compared to other electrode materials employed for the same purposes. Indeed, energy harvesting from acidic wastewater treatment can be a profitable and sustainable practice mainly for industries that generate enormous amounts of wastewater.

INTRODUCTION

Given the growing search for environmentally friendly solutions, developing electrochemical systems based on the variation of ion concentrations in solution has drawn great attention [1-4]. In 1954, Pattle proposed the Hydroelectric Pile, which was the first electrochemical system to involve mixing of river water and seawater as a renewable energy source [2]. In 1974, Norman described a system called Pressure Retarded Osmosis (PRO), composed of osmotic membranes and located between fresh and seawater, for converting energy associated with the difference in osmotic pressure [3]. In 1979, Loeb patented a reverse electrodialysis system coupled to a regeneration unit; for example, a distiller, to convert energy through selective ion permeation and spontaneous redox reactions [4]. In 2009, Brogioli et al. proposed an electrochemical device called capacitive mixing (CapMix) [5], which was based on electrical double-layer capacitors immersed in solutions with different ion concentrations [6]. In 2011, La Mantia et al. proposed electrochemical systems called mixing entropy batteries, which can also be used to harvest energy from faradaic reactions in solutions with different salinity, such as seawater and river water [7]. Since these works were published, new strategies based on variations in ion concentrations have been proposed for energy storage [8].

In this sense, our group has investigated electrochemical systems to generate electrical energy from the variation in proton and alkali metal cation (sodium and potassium ions) concentrations in the course acid solution neutralization [9,10]. A possible practical application of these systems would be generating electrical energy from acidic wastewater. The next section of this paper describes the working principle of these electrochemical systems, the thermodynamic formalism that demonstrates the harvested energy, and the kinetic model.

Implementing these electrochemical systems depends on several parameters that require further investigation; e.g., choosing electrodes with suitable properties for this application. Low electrode reaction irreversibility, chemical stability, and electric potential dependence on the electrolyte solution pH (so that the full cell voltage varies as a function of pH) are essential for energy harvesting [11]. In this way, our group studied proton adsorption/desorption reaction in electrodes formed from self-assembled phosphomolybdic acid films ($H_3PMo_{12}O_{40}$, PMo_{12}) to demonstrate energy harvesting in the course acid solution neutralization. We found that the electrode potential was a function of pH, and that the reactions were fast in aqueous medium, which decreased energy dissipation in the form of heat [11-13].

$$H_3PMo_{12}O_{40}(s) + xe^- + xH^+(aq) \leftrightarrows H_{3+x}PMo_{12-x}^{VI}Mo_x^{V}O_{40}(s) \quad (1),$$

To investigate electrode materials with properties that allow them to be used in more applicable systems, we adsorbed PMo_{12} clusters on carbon black (PMo_{12}/CB) and deposited them on carbon cloth. Consequently, we obtained a larger amount of electroactive material as compared to self-assembled PMo_{12} films, which resulted in 250-times increase of the electric charge (30 $mC.cm^{-2}$) [9,13]. However, the electrochemical performance of PMo_{12}-based materials can be further improved. For example, other support materials can cause the charge storage capacity to increase and overpotentials to decrease [14].

One option is to use reduced graphene oxide (RGO), with a three-dimensional open porous architecture, as support material. D.P. Dubal et al. [14] performed morphological, structural, and compositional analysis of PMo_{12} anchored on three-dimensional RGO and demonstrated that a large amount of PMo_{12} clusters was anchored on the surface of the RGO sheets. In fact, RGO has characteristics that make it suitable not only for our purpose, but also for several other electrochemical energy storage

systems: it has a large surface area and a high electronic mobility at room temperature [15,16]. On the basis of Brunauer-Emmett-Teller (BET) analysis, the PMo_{12}/RGO surface area was calculated as 231 m^2/g, which was close to the RGO surface area (242 m^2/g). Moreover, according to the adsorption-desorption curves, the most probable pore width and volume were 3.48 nm and 0.14 cm^3/g, respectively [17,14]. Thus, when minimum PMo_{12} clusters (1 nm) were dispersed on the surface of RGO sheets at a molecular level [14,17], all the metal moieties were on the cluster surface, and a large number of electroactive sites could be easily accessed by protons (Equation 1) from the electrolyte solution inside and outside the electrode pores, to increase the charge capacity and to decrease overpotentials as compared to other previously investigated electrodes [9, 12].

We also prepared films from copper hexacyanoferrate (CuHCF) and evaluated them as positive electrodes in our electrochemical system to harvest energy from the variation in alkali metal cation concentration in the electrolyte solution [8]. We chose CuHCF on the basis of some characteristics of this electrode material, including chemical stability in acidic medium (electrolyte solution pH equal to or higher than 2) and low practical irreversibility for alkali metal ion intercalation/deintercalation (potassium and sodium ions, for instance) [18-22]. Copper ions octahedrally coordinated to nitrogen atoms of hexacyanometalate groups increase the size of the channels in the hexacyanometalate structure (unit cells with face-centered cubic structure), enhancing the ion insertion rate [19]. In addition, just as the PMo_{12}/RGO electrode must be electroactive with respect to protons, without any effect or with minimum effect of the alkali metal ion concentration, the CuHCF electrode must be electroactive with respect to potassium ions, without any effect or at least without a strong effect of the proton concentration on electrode potential [23]:

$$KCu[Fe(CN)_6](s) + xK^+(aq) + xe^- \leftrightarrows K_{(1+x)}Cu[Fe(CN)_6](s) \quad (2),$$

allowing energy to be harvested. Although protons can also intercalate in the CuHCF structure, potassium ions are preferentially intercalated when the concentration of these ions is higher than or close to the proton concentration in the same electrolyte solution (as observed and shown below for the proton and potassium ion concentrations of the solutions used in this work).

Although PMo_{12} and CuHCF have previously been studied for similar applications [11,24], here we analyze how these materials behave when deposited on other support materials, aiming at their use closer to practical application. More specifically, this work investigates electrochemical reactions of electrode materials consisting of PMo_{12}/RGO and CuHCF powder dispersed in carbon black, both deposited on carbon cloth, in electrolyte solutions with different proton and potassium ion concentrations. Other alkali metal ions could be used, including sodium, lithium, rubidium, and cesium ions. However, potassium ion intercalation/deintercalation in CuHCF is known to have the highest reversibility and rate capability [18,25], which improves the electrochemical system performance, as will be mentioned below. Furthermore, this electrochemical system operates at pH ranging from 2 to 6 due to the chemical stability of the electrodes, as will be shown below. From the models developed in the frequency domain [21,26-28], we propose models for the kinetic study of porous electrodes associated with the proton adsorption/desorption reaction in PMo_{12}/RGO and potassium ion intercalation/deintercalation in CuHCF.

Working principle, thermodynamics, and kinetic model in the frequency domain

The working principle of the electrochemical system proposed here, which operates in four-step cycles and at pH ranging from 2 to 6, is illustrated in Figure 1a and 1b and is described below [24]:

Step I – In this step, saline, buffered, and slightly acidic solution resulting from a previous cycle is removed from the electrochemical cell; instead of it the H_2SO_4 and K_2SO_4 solution is transferred from the acid reservoir to the cell (without allowing it to dry) under open circuit potential. K_2SO_4 is added together with H_2SO_4 to decrease the solution resistance. The latter solution (K_2SO_4 and H_2SO_4) has higher proton and lower potassium ion concentrations than the removed solution. The decrease in voltage associated with the replacement of the former solution in the cell is illustrated in Figure 1b at electric charge (q) equal to zero. The pH of the solution added to the cell in this step should not be equal to or lower than 1, to prevent the CuHCF electrode from decomposing, as will be discussed below.

Step II – This step involves simultaneous electron flow from the positive to the negative electrode through the external circuit and ion flow from the positive (CuHCF) to the negative (PMo_{12}/RGO) electrode through the solution, which requires electrical energy from the external electrical source to be spent (non-spontaneous process). In this case, n_e mol of protons is transferred from the acid solution (containing n_{H^+} mol of protons and n_{K^+} mol of potassium ions after step I) to the negative electrode, and n_e mol of potassium ions is transferred from the positive electrode to the acid solution:

$$H_3PMo_{12}O_{40}(s) + K_{(1+x)}Cu[Fe(CN)_6](s) + xH^+(aq) \rightarrow$$

$$H_{3+x}PMo_{12}O_{40}(s) + KCu[Fe(CN)_6](s) + xK^+(aq) \quad (3)$$

In this step, the charge changes from zero to its maximum value ($q_{max} = Fn_e$, where F is the Faraday constant. q_{max} is related to the maximum amount of potassium ions inside the CuHCF electrode), and the voltage is expected to increase progressively because the proton concentration and the potassium ion concentration in the solution decreases and

increases during the electrochemical reaction, respectively (Equation 3). However, these concentration variations can be minimized if n_{H^+} and n_{K^+} are much greater than n_e.

Step III – In this step, KOH, CH_3COOK, and K_2SO_4 from the basic reservoir are added to the acid solution inside the electrochemical cell under open circuit potential, where the voltage increases at a charge equal to q_{max} because the proton concentration in the solution decreases due to the neutralization reaction:

$$H_2SO_4(aq) + 2KOH(aq) \rightarrow 2H_2O\ (l) + K_2SO_4(aq) \quad (4),$$

and buffer formation (for slightly acidic solution):

$$CH_3COO^-(aq) + H^+(aq) \Leftrightarrow CH_3COOH\ (aq) \quad (5).$$

In addition, the potassium ion concentration in the solution increases, increasing the voltage. After step III, the solution in the cell should not be neutral, to prevent the PMo_{12}/RGO electrode from decomposing, or alkaline, to prevent both the electrodes used here from being decomposed, as will be discussed below. This justifies the choice of acetate buffer.

The number of mol of base (n_b) that should be added in this step is calculated so that the solution inside the cell reaches a desired pH at the end of the cycle (after step IV). The n_{H^+} value in the slightly acidic solution inside the cell after step II and the number of mol of buffer conjugate base (n_{Ac}) that has been added to the solution. The presence of buffer conjugate base (CH_3COOK) reduces the solution pH variation in step IV, and its amount depends on the value of n_e mol of protons that is electrochemically transferred to the solution in the following step. Meanwhile, excess K_2SO_4 in the solution increases the potassium ion concentration, consequently enhancing energy harvesting, as will be discussed below.

Step IV – In this step, the electrochemical cell is allowed to discharge spontaneously. The electrons flow from the negative (PMo_{12}) to the positive (CuHCF) electrode through external circuit, which contains a system for storing energy; n_e mol of protons are

transferred from the negative electrode to the solution, and n_e mol of potassium ions are transferred from the solution to the positive electrode:

$$H_{3+x}PMo_{12}O_{40}(s) + KCu[Fe(CN)_6](s) + xK^+(aq) + xCH_3COO^-(aq) \rightarrow$$

$$H_3PMo_{12}O_{40}(s) + K_{(1+x)}Cu[Fe(CN)_6](s) + xCH_3COOH(aq) \quad (6)$$

In this step, the charge changes from q_{max} to zero, and minimum progressive decrease in the voltage (associated with the variation in the proton and potassium ion concentrations in solution) is expected due to the buffer and excess K_2SO_4 in the slightly acidic solution ($n_{K^+} >> n_e$).

After step IV, the solution containing the saline, buffered, and slightly acidic solution is taken away from the cell; base is added to restore the buffer conjugate base (CH_3COOK), so that K_2SO_4 can be separated from KOH and CH_3COOK during water evaporation due to the difference in water solubility (11.1 g/100 mL, 121.0 g/100 mL, and 268.6 g/100 mL for K_2SO_4, KOH, and CH_3COOK at 25 ºC, respectively [29]). Part of the recovered K_2SO_4 can be added to the acid reservoir, and the remaining K_2SO_4, together with KOH and CH_3COOK, can be added to the basic reservoir. As for the cell, a new portion of the H_2SO_4 and K_2SO_4 solution is inserted so that the system is ready to repeat the cycle from Step I.

The concentration of the chemical species in the basic reservoir depends on several factors, such as the pH of the acid solution in the acid reservoir; the cell volume and the acid solution volume added to the cell during step I; the solution volume (or the solid mixture mass) added to the cell in step III; and the desired n_e, n_{H^+}, n_{K^+}, n_b, and n_{Ac} values throughout the cycle. As an example, this work will show the composition of the solution inside the electrochemical cell after each step for the experimental conditions used here and, consequently, the amount of KOH, CH_3COOK, and K_2SO_4 (of the basic reservoir) added to the solution.

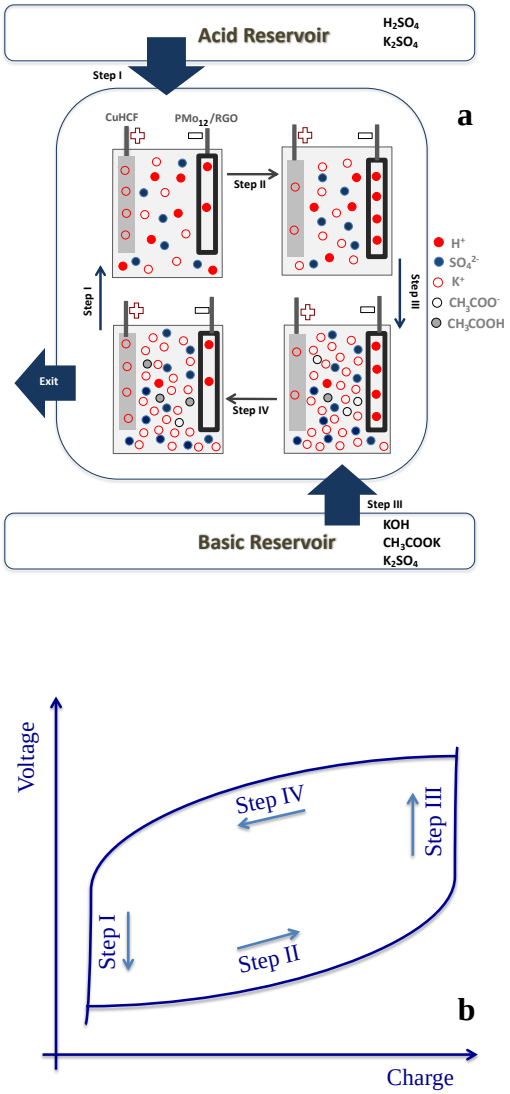

Figure 1 – a) Working principle of the electrochemical system; b) Schematic profile of the charge/discharge curves.

According to the working principle shown above, protons are transferred from the solution with higher proton activity (a_{H^+}) to the solution with lower a_{H^+}. Similarly, potassium ions are transferred from the solution with higher potassium ion activity (a_{K^+}) to the solution with lower a_{K^+}. In this way, at constant temperature and pressure, the maximum energy harvested after the cycle corresponds to the mixture free energy (ΔG_{mix}). Hence, the harvested energy corresponds to the difference between ΔG_{mix} and the energy dissipated in the form of heat (Q). As shown in Figure 1b, the line integral computes this harvested energy along pathways from steps I to IV.

If the electrochemical reactions related to the negative (PMo_{12}/RGO) and positive (CuHCF) electrodes only involve protons and potassium ions, respectively, according to Equations 3 and 4, the electromotive force (E_{rxn}) is a function of the proton and potassium activities, and the harvested energy normalized by the number of mol of protons (or potassium ions) that participate in the isothermal electrochemical reactions (ε) corresponds to

$$\varepsilon = \int_0^1 F\Delta E d\left(\frac{q}{q_{max}}\right) = \frac{-(\Delta G_{mix} - Q)}{n_e} = -\int_0^1 (\Delta G_r^{II} + \Delta G_r^{IV}) d\left(\frac{\xi}{n_e}\right) + \frac{Q}{n_e} = \int_0^1 F(E_{rxn}^{II} + E_{rxn}^{IV}) d\left(\frac{q}{q_{max}}\right) - \int_0^1 F(|\eta^{II}| + |\eta^{IV}|) d\left(\frac{q}{q_{max}}\right) =$$

$$RT\int_0^1 \ln\left(\frac{a_{M_1}^{IV} a_{KM_1}^{II} a_{M_2}^{II} a_{HM_2}^{IV} a_{K^+}^{IV} a_{H^+}^{II}}{a_{M_1}^{II} a_{KM_1}^{IV} a_{M_2}^{IV} a_{HM_2}^{II} a_{K^+}^{II} a_{H^+}^{IV}}\right) d\left(\frac{q}{q_{max}}\right) - \int_0^1 F(|\eta^{II}| + |\eta^{IV}|) d\left(\frac{q}{q_{max}}\right) \quad (7),$$

where n_e corresponds to the number of mol of electrochemically adsorbed protons (or electro-deintercalated potassium ions); ΔG_r is the electrochemical reaction free energy; ξ is the reaction extent; R is the ideal gas constant; T is the absolute temperature; F is the Faraday constant; η is the overpotential; ΔE is the potential difference; i is the electric current; and "a" is the activity. The superscripts II and IV refer to steps II and IV. The subscripts M_1, KM_1, M_2, and HM_2 refer to $KCu[Fe(CN)_6]$, $K_{(1+x)}Cu[Fe(CN)_6]$, $H_3PMo_{12}O_{40}$, and $H_{3+x}PMo_{12}O_{40}$, respectively, while a_{H^+} and a_{K^+} correspond to the proton activity and potassium ion activity, respectively.

All these activities are functions of the reaction extent (ξ = q/F) and vary along the charge/discharge processes. However, when n_{H^+} and n_{K^+} are much higher than n_e in step II, and n_{Ac} and n_{K^+} are much higher than n_e in step IV, the proton and potassium ion activities remain virtually constant along these steps, and Equation 7 becomes

$$\varepsilon = RT\ln\left(\frac{a_{K^+}^{IV}}{a_{K^+}^{II}}\frac{a_{H^+}^{II}}{a_{H^+}^{IV}}\right) + RT\int_0^1 \ln\left(\frac{a_{M_1}^{IV} a_{KM_1}^{II} a_{M_2}^{II} a_{HM_2}^{IV}}{a_{M_1}^{II} a_{KM_1}^{IV} a_{M_2}^{IV} a_{HM_2}^{II}}\right) d\left(\frac{q}{q_{max}}\right)$$

$$-\int_0^1 F(|\eta^{II}| + |\eta^{IV}|)d\left(\frac{q}{q_{max}}\right) \quad (8).$$

Unlike other systems that harvest energy from the difference in ion concentrations [5,7], in our case the total amount of ions in solution can remain constant throughout the cycle (because the pH of the solution is lower than 7 after step III): the number of protons transferred to/from the negative electrode is equivalent to the number of potassium ions deintercalated/intercalated from/in the positive electrode in step II/step IV, which corresponds to the n_e value; the number of protons that reacts with hydroxyl anions to form water molecules is equivalent to the number of potassium ions from the base that is added to the cell solution in step III. Thus, depending on the ion concentrations in the electrochemical cell solution, which is related to the ion concentrations in the solution in the acid reservoir and the amount of base added from the basic reservoir, the energy dissipation associated with the resistance of the solution can be significantly reduced. In our case, we have even added more salt in step III because, the higher the potassium ion concentration in the solution during step IV as compared to step II, the greater the harvested energy (Equation 7 or 8) [9]. For this reason, we have also added salt close to its saturation in water in step III, as will be shown below.

According to the working principle and the data shown below, we have been able to predict the composition of the solutions inside the electrochemical cell after each step (table 1). This was done on the basis of the number of mol of the chemical species that participated in steps I to IV (for j = 0.1 mA.cm^{-2} and A = 1 cm^2). We assumed that the solution volume (20 mL) in the electrochemical cell was constant during the cycle even when solid KOH, CH_3COOK, and K_2SO_4 were added from the basic reservoir. After step I, the n_{H^+} value referred to pH = 2. When 4.39 x 10^{-7} mol of electrons (n_e = 42.4 mC/F) passed through the external circuit (step II), from the CuHCF electrode to the PMo_{12}/RGO electrode, 4.39 x 10^{-7} mol of protons adsorbed on the PMo_{12}/RGO electrode, and the same amount (n_e mol) of potassium ions was transferred from the CuHCF electrode to the

solution. Observe that, after step II, the number of mol of protons and potassium ions in solution practically did not change when compared to the end of step I because n_{H^+} and n_{K^+} were much higher than n_e. When 2.93 x 10^{-4} mol of KOH, 1.75 x 10^{-4} mol of CH_3COOK, and 2.0 x 10^{-2} mol of K_2SO_4 were added to the solution, the pH solution was 6 (n_{H^+} = 2 x 10^{-8}) after step III. When 4.31 x 10^{-7} mol of electrons (q = 41.6 mC) passed through the external circuit (step IV) from the PMo_{12}/RGO electrode to the CuHCF electrode, 4.39 x 10^{-7} mol of protons was transferred from the PMo_{12}/RGO electrode to the solution, and the same amount of potassium ions was transferred from the solution to the CuHCF electrode. Observe that n_{H^+} and n_{K^+} after step IV practically did not change when compared to the values obtained after step III because n_{Ac} and n_{K^+} were much higher than n_e. Thus, the cell voltage practically did not vary as a function of the proton and potassium ion concentrations. Although the n_e/n_{H^+} ratio should be higher to increase the energy harvested per volume unit of the acid solution (given that a greater amount of electric charge could be involved in electrochemical processes per unit volume of acid solution added to the cell), and to make this system suitable for practical applications, our interest here was only to estimate the maximum energy harvested per mol of adsorbed proton, to allow us to evaluate the electrochemical properties of the electrodes. For n_e values close to n_{H^+} values (assuming pH equal to 2 after step I), electrochemical cells must be designed to accommodate smaller amounts of solution.

Table 1 – Predicted compositions of the solutions (in mol) for the full electrochemical cell throughout the cycle. V = 20 mL and j = 0.1 mA.cm^{-2} (q_{max} = 42.4 mC).

	$\mathbf{n_{H^+}}$ /mol	$\mathbf{n_{K^+}}$ /mol	n_a/mol[b]	n_e/mol	n_{Ac}/mol	n_{HAc}/mol
After Step I[a]	3.03 x 10^{-4}	8.00 x 10^{-4}	7.2 x 10^{-4}	-	-	-
After Step II	3.02 x 10^{-4}	8.00 x 10^{-4}	7.2 x 10^{-4}	4.39 x 10^{-7}	-	-
After Step III	2.00 x 10^{-8}	2.08 x 10^{-2}	1.07 x 10^{-2}	-	1.65 x 10^{-4}	9.30 x 10^{-6}
After Step IV	2.10 x 10^{-8}	2.08 x 10^{-2}	1.07 x 10^{-2}	4.31 x 10^{-7}	1.64 x 10^{-4}	9.73 x 10^{-6}

[a] The activity coefficients for H^+, HSO_4^-, and SO_4^{2-} were 0.66, 0.66, and 0.54, respectively [30,31].
[b] n_a is the sum of the number of moles of SO_4^{2-} and HSO_4^- in solution.

To understand the electrochemical steps accounting for overpotentials better, we have developed a kinetic model in the frequency domain on the basis of other models associated with charge transfer, adsorption, and mass transport in particles and films [21,26,27], whose transfer function can be inserted into the porous electrode model [28]. Consequently, according to the proposed reaction mechanism, the rate constants and the diffusion coefficient can be determined from the electrochemical impedance data for porous electrodes.

According to the Maclaurin series, the oscillating faradaic current $\tilde{\imath}_f$ can be expressed as a function of the oscillating potential ($\widetilde{E}$) and the degree of coverage of electroactive sites ($\tilde{\theta}$) due to the adsorption reaction represented in Equation 1:

$$\tilde{\imath}_f = \left(\frac{\partial \bar{\imath}_f}{\partial \bar{E}}\right)_{\bar{\theta}} \widetilde{E} + \left(\frac{\partial \bar{\imath}_f}{\partial \bar{\theta}}\right)_{\bar{E}} \tilde{\theta} \qquad (9),$$

where $\bar{\imath}_f$, $\bar{E}$, and $\bar{\theta}$ are the faradaic current density, potential, and degree of coverage, respectively. The "~" and "–" superscripts correspond to oscillating and steady state states, respectively.

By considering Equation 1 as an elementary step, and assuming that the adsorption reaction follows the Langmuir isotherm, which is characterized by the degree of coverage ($\bar{\theta}$) of electroactive sites, $\bar{\imath}_f$ can be expressed as:

$$\bar{\imath}_f = \bar{\imath}_{f,a} + \bar{\imath}_{f,d} = -Fk_1(1-\bar{\theta})e^{-\beta b\bar{\eta}} + Fk_1'\bar{\theta}e^{(1-\beta)b\bar{\eta}} \qquad (10)$$

where $\bar{\imath}_{f,a}$ and $\bar{\imath}_{f,d}$ are the faradaic current densities associated with the adsorption and desorption reactions, respectively; k_1 (= kC_{H^+}) and k_1' are the rate constants for the adsorption and desorption reactions, respectively; $C_{H^+}$is the proton concentration; $b = F/RT$; $\bar{\eta}$ is the overpotential; and β is the symmetry factor. Substituting Equation 10 in Equation 9, $\tilde{\imath}_f$ can be given by

$$\tilde{i}_f = \tilde{i}_{f,a} + \tilde{i}_{f,d} = \left(Fk_1(1-\bar{\theta})\beta b e^{e^{-\beta b\bar{\eta}}} + Fk_1'\bar{\theta}(1-\beta)be^{(1-\beta)b\bar{\eta}}\right)\tilde{E} +$$

$$\left(Fk_1 e^{-\beta b\bar{\eta}} + Fk_1' e^{(1-\beta)b\bar{\eta}}\right)\tilde{\theta} \quad (11).$$

Assuming that $i_{f,a} < 0$ and $i_{f,d} > 0$, the faradaic current density can be associated with the temporal variation of the degree of coverage:

$$\Gamma F\frac{d\theta}{dt} = -i_f = -(i_{f,a} + i_{f,d}) \quad (12).$$

Meanwhile, the faradaic current density (i_f) can be related to the oscillating degree of coverage in the frequency domain:

$$\tilde{i}_f = \tilde{i}_{f,a} + \tilde{i}_{f,d} = -\Gamma Fj\omega\tilde{\theta} \quad (13),$$

where Γ is the maximum surface concentration of the electroactive sites at a *dc* potential; j is the imaginary unit; and ω is the angular frequency. To determine the oscillating faradaic impedance, the oscillating degree of coverage should be explicit as a function of the oscillating potential. Substituting Equation 13 in Equation 11,

$$\tilde{\theta} = \frac{Fk_1(1-\bar{\theta})\beta b e^{-\beta b\bar{\eta}} + Fk_1'\bar{\theta}(1-\beta)be^{(1-\beta)b\bar{\eta}}}{-(\Gamma Fj\omega + Fk_1 e^{-\beta b\bar{\eta}} + Fk_1' e^{(1-\beta)b\bar{\eta}})}\tilde{E} \quad (14)$$

and inserting the oscillating degree of coverage of Equation 14 in Equation 11, we obtain the faradaic impedance ($Z_f^{-1} = \frac{\tilde{i}_f}{\tilde{E}}$):

$$Z_f^{-1} = \left(Fk_1(1-\bar{\theta})\beta b e^{e^{-\beta b\bar{\eta}}} + Fk_1'\bar{\theta}(1-\beta)be^{(1-\beta)b\bar{\eta}}\right) -$$

$$\left(Fk_1 e^{-\beta b\bar{\eta}} + Fk_1' e^{(1-\beta)b\bar{\eta}}\right)\left(\frac{Fk_1(1-\bar{\theta})\beta b e^{-\beta b\bar{\eta}} + Fk_1'\bar{\theta}(1-\beta)be^{(1-\beta)b\bar{\eta}}}{\Gamma Fj\omega + Fk_1 e^{-\beta b\bar{\eta}} + Fk_1' e^{(1-\beta)b\bar{\eta}}}\right) \quad (15).$$

In these electrochemical systems, the different values of x in Equations 1 and 2 correspond to different equilibrium states, and the steady states correspond to these equilibrium states [21]. Therefore, we consider the overpotentials at the steady states equal to zero, so Equation 15 can be expressed as follows:

$$Z_f = \frac{1}{R_{ct}^{-1}\left(1-\frac{Fk_1+Fk_1'}{j\omega\Gamma F+Fk_1+Fk_1'}\right)} = \frac{1}{R_{ct}^{-1}\left(1-\frac{1}{1+j\omega\frac{\Gamma}{k_1+k_1'}}\right)} = R_{ct}\left(1+\frac{1}{j\omega\frac{\Gamma}{k_1+k_1'}}\right) \quad (16)$$

$$R_{ct} = \frac{1}{[Fk_1 b\beta(1-\bar{\theta})+Fk_1' b\bar{\theta}(1-\beta)]} \quad (17)$$

where R_{ct} is the charge transfer resistance. We can determine the kinetic constants on basis of the $\Gamma/(k_1+k_1^{-1})$ ratio and R_{ct} values, determined from fitting of the impedance data (as will be shown below); Langmuir's isotherm; $\bar{q}$ electrical charge related to the electro-reduction of PMo_{12} sites (responsible for the change in the equilibrium state of the PMo_{12}/RGO electrode corresponding to fully oxidized, $\bar{q} = 0$, to more reduced, $\bar{q} > \bar{0}$); and Equation 18

$$\Gamma\bar{\theta} = \frac{n_{ads}}{A} = \frac{\bar{q}}{FA} \quad (18),$$

where n_{ads} is the number of mol of occupied electroactive adsorption sites. As will be shown below, the electrode equilibrium potential is a function of $\bar{q}$; that is, the adsorption site energy distribution is wide. Hence, the Γ and $\bar{\theta}$ values only consider the sites that are thermodynamically favorable for adsorption at the equilibrium state corresponding to the applied *dc* potential.

In the case of Equation 2, the oscillating faradaic current can be expressed as a function of the oscillating potential and potassium ion concentration gradient ($\tilde{C}'$) in the host matrix:

$$\tilde{I}_f = \left(\frac{\partial \bar{I}_f}{\partial \bar{E}}\right)_{\bar{\theta}} \tilde{E} + \left(\frac{\partial \bar{I}_f}{\partial \bar{C}'}\right)_{\bar{E}} \tilde{C}' \quad (19),$$

where $\bar{C}'$ is the concentration gradient at the steady state. By using Fick's first and second law, the current-overpotential equation, and the suitable initial and boundary conditions for potassium ion insertion into the CuHCF electrode [21], the faradaic impedance can be expressed as

$$Z_f = \frac{RT}{\alpha F^2 k} + \left|\frac{2L\left[\cosh^2\left(\omega^{\frac{\gamma}{2}}\sqrt{\frac{L^2}{2D}}\right)\cos^2\left(\omega^{\frac{\gamma}{2}}\sqrt{\frac{L^2}{2D}}\right)+\sinh^2\left(\omega^{\frac{\gamma}{2}}\sqrt{\frac{L^2}{2D}}\right)\sin^2\left(\omega^{\frac{\gamma}{2}}\sqrt{\frac{L^2}{2D}}\right)\right]}{C_L D^{\frac{1}{2}}\omega^{\frac{\gamma}{2}}\sqrt{\sinh^2\left(2\omega^{\frac{\gamma}{2}}\sqrt{\frac{L^2}{2D}}\right)+\sin^2\left(2\omega^{\frac{\gamma}{2}}\sqrt{\frac{L^2}{2D}}\right)}}\right| \cos\left(\arctan\left(\frac{\sinh\left(2\omega^{\frac{\gamma}{2}}\sqrt{\frac{L^2}{2D}}\right)+\sin\left(2\omega^{\frac{\gamma}{2}}\sqrt{\frac{L^2}{2D}}\right)}{\sinh\left(2\omega^{\frac{\gamma}{2}}\sqrt{\frac{L^2}{2D}}\right)-\sin\left(2\omega^{\frac{\gamma}{2}}\sqrt{\frac{L^2}{2D}}\right)}\right)\right) -$$

$$j^{\gamma}\left|\frac{2L\left[\cosh^2\left(\omega^{\frac{\gamma}{2}}\sqrt{\frac{L^2}{2D}}\right)\cos^2\left(\omega^{\frac{\gamma}{2}}\sqrt{\frac{L^2}{2D}}\right)+\sinh^2\left(\omega^{\frac{\gamma}{2}}\sqrt{\frac{L^2}{2D}}\right)\sin^2\left(\omega^{\frac{\gamma}{2}}\sqrt{\frac{L^2}{2D}}\right)\right]}{C_L D^{\frac{1}{2}}\omega^{\frac{\gamma}{2}}\sqrt{\sinh^2\left(2\omega^{\frac{\gamma}{2}}\sqrt{\frac{L^2}{2D}}\right)+\sin^2\left(2\omega^{\frac{\gamma}{2}}\sqrt{\frac{L^2}{2D}}\right)}}\right| \sin\left(\arctan\left(\frac{\sinh\left(2\omega^{\frac{\gamma}{2}}\sqrt{\frac{L^2}{2D}}\right)+\sin\left(2\omega^{\frac{\gamma}{2}}\sqrt{\frac{L^2}{2D}}\right)}{\sinh\left(2\omega^{\frac{\gamma}{2}}\sqrt{\frac{L^2}{2D}}\right)-\sin\left(2\omega^{\frac{\gamma}{2}}\sqrt{\frac{L^2}{2D}}\right)}\right)\right) \quad (20).$$

where D is the diffusion coefficient; L is the host matrix thickness, $\frac{d\bar{q}}{d\bar{E}}$ is the limiting capacitance C_L; and ϕ is the phase angle related to the diffusion process. Considering that the oscillating potential is low, we do not consider the mass transport associated with the electric potential gradient inside the particles because the electron-ion pair tends to be close, and electroneutrality is maintained [32]. Thus, we consider only the mass transport associated with electron-ion pair diffusion [21].

We then insert non-faradaic parameters like the double-layer capacitance (C_{dl}) in parallel to faradaic impedances Z_f (Equations 16 and 20 associated with Equations 1 and 2, respectively) and the dimensionless term β (associated with frequency dispersions [33]) into the transfer function:

$$Z_p(\omega) = \frac{Z_f(\omega)}{1+(j\omega)^{\beta} C_{dl} Z_f(\omega)} \quad (21)$$

Here, the electrodes consisting of PMo_{12}/RGO and CuHCF dispersed in carbon black and deposited on carbon cloth are porous. Tröltzsch and Kanoun proposed a general transmission line, which assumes an electronic (solid electrode material) and an ionic (electrolyte solution in the electrode pores) conduction phase, as well as a charge transfer

reaction between them. The total impedance involving the porous electrode (Z_{el}) includes the Z_p transfer function associated with the faradaic reactions [28]:

$$Z_{el} = R_0 + \frac{L_{el}}{A_{el}(\sigma+\kappa)}\left(1 + \frac{2+\left(\left(\frac{\kappa}{\sigma}\right)+\left(\frac{\sigma}{\kappa}\right)\right)\cosh\left(L_{el}\sqrt{\frac{\kappa+\sigma}{\sigma\kappa}\left(\frac{Zp}{a}\right)}\right)}{\left(L_{el}\sqrt{\frac{\kappa+\sigma}{\sigma\kappa}\left(\frac{Zp}{a}\right)}\right)\text{senh}\left(L_{el}\sqrt{\frac{\kappa+\sigma}{\sigma\kappa}\left(\frac{Zp}{a}\right)}\right)}\right) \quad (22)$$

where κ is the effective conductivity of the solution inside the pores; σ is the effective conductivity of the solid material; "a" is the ratio between the particle area and the electrode volume; L_{el} is the electrode thickness; A_{el} is the porous electrode area (1 cm^2); and R_0 is the sum of resistances in series (R_0) present in the electrochemical system (bulk electrolyte solution, current collector, and contact resistances).

EXPERIMENTAL

CuHCF was synthesized by the co-precipitation method [18]. To this end, 100 mL of 25 mM $Cu(NO_3)_2$ (Sigma-Aldrich) and 100 mL of 25 mM $K_3Fe(CN)_6$ (Acros Organics) were simultaneously and slowly added to 200 mL of deionized water to a constant stoichiometric ratio. These precursors were allowed to react in water, and the precipitate was filtered off, washed with water, and dried at 120 ^oC under vacuum.

Graphene oxide (GO) was synthesized from natural graphite by using the modified Hummers method. Briefly, 2.5 g of $NaNO_3$ and 125 mL of H_2SO_4 were added to 2.5 g of graphite and stirred for 30 min in an ice bath. Then, 12.5 g of $KMnO_4$ was added to the resulting solution, which was stirred at 50 ^oC for 2 h. Next, 500 mL of deionized water and 15 mL of H_2O_2 (35%) were slowly added to the solution, which was washed with dilute HCl. The GO product was washed again with 250 mL of concentrated HCl (37%). Reduced graphene oxide (RGO) was prepared by treating the GO sample at 800 ^oC under nitrogen for 1 h [34].

To prepare the PMo_{12}/RGO composite, 0.25 g of RGO was dispersed in 50 mL of deionized water with a probe sonicator (1000 watts) for 30 min. Then, PMo_{12} was added to 50 mL of the pre-sonicated RGO dispersion. While Dubal et al. [14] used different PMo_{12} concentrations and observed polyoxometalate saturation on the surface of the carbonaceous support material for RGO dispersion with 10 mM PMo_{12}, a result of the limited number of functional groups on the RGO surface, only this PMo_{12} concentration was used here, which guaranteed the maximum number of PMo_{12} clusters in the composite. This suspension was further sonicated (bath sonicator; 200 W) for 2 h and kept at room temperature for 24 h. After that, the composite was filtered off and dried in a vacuum oven at 80 ^{o}C overnight.

Scanning transmission electron microscopy (STEM) was carried out on the Tecnai G2 F20 S-TWIN HR(S) TEM-FEI equipment connected with Energy Dispersive X-ray (EDAX) analysis. More details about the morphology of the PMo_{12}/RGO composite can be seen in Ref. [14,17], which presents scanning electron microscopy and high-resolution transmission electron microscopy images. The exact mechanism underlying the composite structure is unknown. However, formation of the hybrid material is demonstrated in these references. The crystal structure, oxidation state, pore size distribution, and surface area, among other properties, were investigated by X-ray diffraction (XRD), X-ray photoelectron spectroscopy (XPS), and the Brunauer-Emmett-Teller instrument, respectively, and published in Ref. [14,17], which also contain more details about the preparation of the composite. The CuHCF powder was characterized by XRD measurements, recorded on a Siemens D5005 diffractometer operating with monochromatic Cu-K_a radiation. Thermal gravimetric analysis (TGA) was conducted on the TA Instruments SDT2960 DTA-TGA Simultaneous equipment.

The CuHCF and PMo_{12}/RGO electrodes were prepared by mixing the corresponding solid with carbon black (Super P® Conductive, 99+ %) and polyvinylidene

fluoride (PVDF, Tecaflon) at an 80:10:10 ratio, which was followed by dispersion in 1-methyl-2-pyrrolidinone (0.1 mL for every 33 mg of the mixture of solids, Sigma-Aldrich). The dispersions were agitated for 12 h and deposited (by doctor-blade technique) on carbon cloth. These electrodes were then dried at 80 ^{o}C for one day. The geometrical surface area of the electrodes was equal to 1cm^2.

The electrochemical experiments were carried out on an Autolab PGSTAT30 potentiostat/galvanostat. A platinum gauze and Ag/AgCl in saturated KCl were used as the counter and reference electrodes, respectively. For the experiment involving proton and potassium ion concentration variation, H_2SO_4 (Sigma-Aldrich) and K_2SO_4 (Sigma-Aldrich) electrolyte solutions were added or exchanged by means of a four-channel peristaltic pump model BT100-1F acquired from LongerPump (maximum volumetric flow rate equal to 500 mL/min). The electrochemical cell volume was 30 mL. The distance between the working electrode and the reference electrode was 1.0 cm. Then, 20 mM K_2SO_4 solution (20 mL) at pH = 2 was added to the electrochemical cell for approximately 12 s (volumetric flow rate equal to 100 mL/min), which corresponds to step I of the working principle shown above.

The electrolyte solutions at pH = 6 were buffered by adding 10 μL CH_3COOH (Sigma-Aldrich) and 26.2 mg KOH (Sigma-Aldrich) in 20 mM K_2SO_4 solution (20 mL) at pH = 2, to avoid changes in solution pH during the electrochemical reactions. K_2SO_4 (1.6 g) was also added to this electrolyte solution to enhance energy harvesting (which resulted in 500 mM K_2SO_4 solution at pH = 6), as mentioned earlier and described in Ref. [9], simulating the salt recovered from previous cycles. The duration of this procedure was approximately 1 min, which corresponds to step III of the working principle. The ac electrochemical impedance spectroscopy was carried out between 100 kHz and 10 mHz; the ac amplitude was 5 mV. The Mapple software was used to fit the Nyquist diagrams.

RESULTS AND DISCUSSION

To obtain more details on the distribution of PMo_{12} clusters in rGO sheets, we recorded the PMo_{12}/RGO composite STEM image (Figure 2a). The small white dots represent the PMo_{12} clusters, which were evenly distributed on the RGO with minimal or no apparent agglomeration. This contributed to the decreased overpotentials in the electrochemical processes: proton access to the PMo_{12} electroactive sites was facilitated. A better morphological description of the composite can be seen in Ref. [14,17]. Figure 2b depicts the STEM image of CuHCF, which consisted of agglomerated spherical particles with diameters close to 50 nm. The planar regions were related to the growth of unit cells with face-centered cubic structure, which contained channels for potassium electroinsertion in the distorted polyhedra [19].

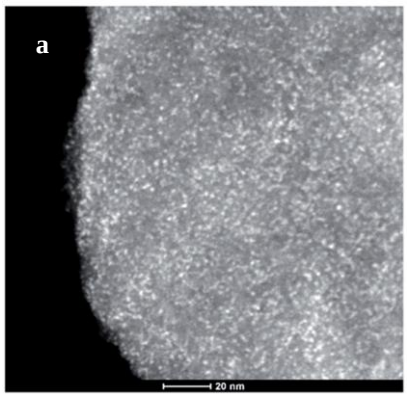

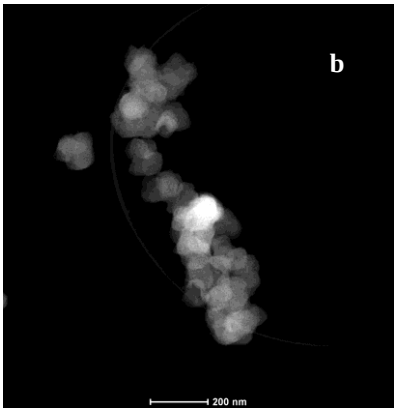

Figure 2 - STEM images of (a) PMo_{12}/RGO (Reproduced from Ref. [17] with permission from the Royal Society of Chemistry) and (b) CuHCF.

The EDS signals associated with molybdenum atoms unambiguously confirmed that PMo_{12} were present on RGO (Figure 3a). Meanwhile, the EDS spectrum confirmed that Cu and Fe were present in the CuHCF structure (Figure 3b). TGA measurements for PMo_{12}/RGO (Figure 3c) pointed to three mass loss steps: a) adsorbed and crystallization water loss below 100 ºC; b) carbon combustion between 450 and 500 ºC; and c) partial PMo_{12} thermal decomposition at higher temperatures [35]. These TGA results enabled us to determine the amount of inorganic compound in the composite (7.0% w/w). Figure 3d shows the XRD for CuHCF. The peaks at 2θ 15.14°, 17.70°, 24.80°, 35.32°, 39.62°, 43.54°, 45.75°, 50.74°, 50.10°, and 57.26° referred to the planes (111), (200), (220), (400), (420), (422), (511), (440), (600), and (620) and indicated that CuHCF had face-centered cubic (FCC) structure [36].

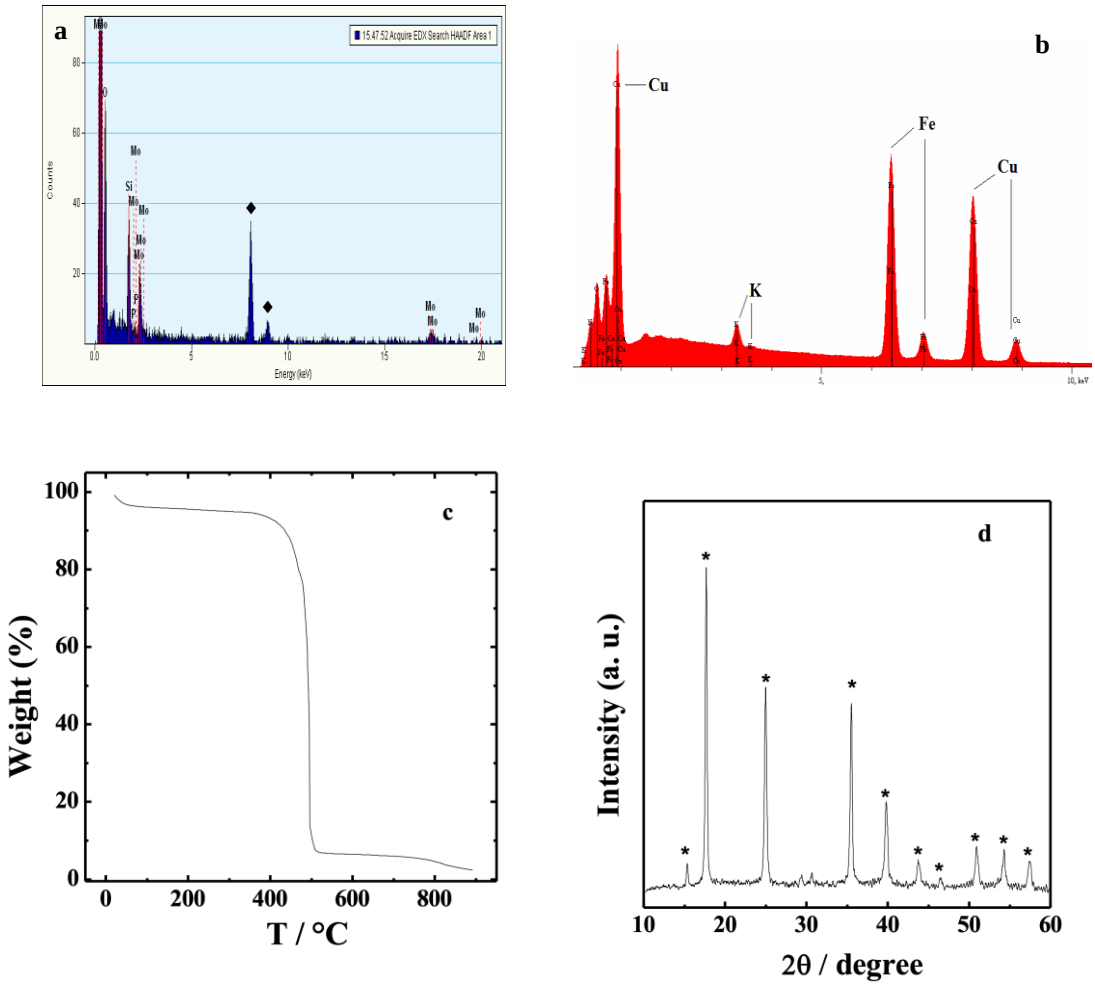

Figure 3 - EDS spectrum of (a) PMo_{12}/RGO and (b) CuHCF. (c) TGA curve of PMo_{12}/RGO. (d) XRD pattern of the CuHCF powder. (♦) The EDX signals associated with copper atoms from the TEM grid. (*) The EDX signals associated with CuHCF.

As shown in Equations 7 and 8, greater variation in the electrolyte solution pH should allow more energy to be harvested. Although the electrodes investigated here present suitable properties for the proposed electrochemical system, these materials are not chemically stable in certain pH ranges. Figures 4a and 4b show linear sweeps for the PMo_{12}/RGO electrode in solutions at different pH. Figure 4a shows a linear sweep toward more negative potentials in 20 mM K_2SO_4 solution at pH = 2. After we exchanged the solution for another 20 mM K_2SO_4 solution at pH = 6, we performed a linear sweep toward more positive potentials. We repeated this procedure twice, and the current values practically did not change. Meanwhile, Figure 4b shows linear sweeps toward more

negative potentials in 20 mM K_2SO_4 solution at pH = 2, followed by another linear sweep toward more positive potentials in 20 mM K_2SO_4 solution at pH = 7. The oxidation current decreased significantly at this pH value. We also repeated this procedure twice. The electric current decreased in relation to the electric current observed in the first linear sweep at pH = 2, demonstrating that the electrode decomposed at pH = 7 probably because PMo_{12} underwent hydrolysis [37]. At pH lower than 2, there is no decomposition [35].

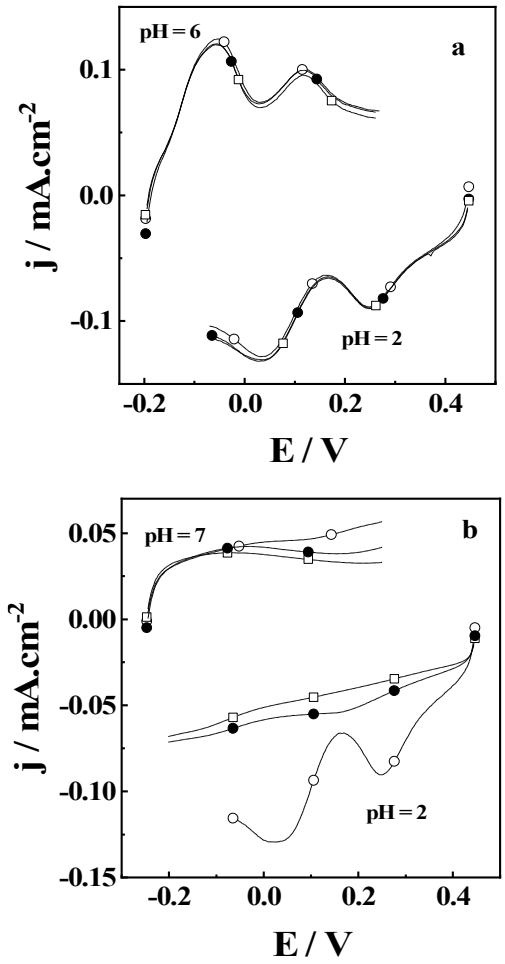

Figure 4 – 1st (—○—), 2nd (—●—), and 3rd (—□—) cycle of linear sweeps toward more negative potentials for the PMo_{12}/RGO electrode at pH = 2, followed by linear sweep toward more positive potentials at pH a) 6 and b) 7. The pH solution is shown in Figures. ν = 1 $mV.s^{-1}$.

Figure 5 shows the equilibrium potential as a function of the charge normalized by the maximum charge associated with proton adsorption/desorption in the PMo_{12}/RGO electrode, according to Equation 1, at pH = 2.0 and at pH = 6.0. The electric potential depended on the solution pH and, from the area between these curves multiplied by the Faraday constant, we obtained the maximum energy harvested per mol of adsorbed proton (7.4 kJ mol^{-1}), which corresponded to the contribution of the mixture free energy per mol of adsorbed proton due to variation in the electrolyte solution pH.

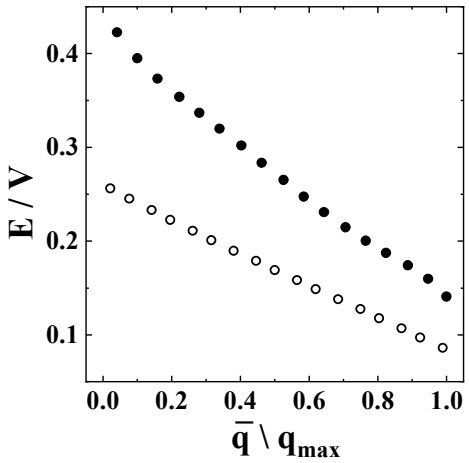

Figure 5 – Measured PMo_{12}/RGO electrode equilibrium potential as a function of normalized charge in (●) 20 mM K_2SO_4 at pH = 2 and (○) 500 mM K_2SO_4 at pH = 6. q_{max} = 42 mC. PMo_{12} mass = 0.25 mg. A = 1 cm^2.

Figure 6 illustrates the PMo_{12}/RGO electrode reduction and oxidation curves in 20 mM K_2SO_4 at pH = 2 and in 500 mM K_2SO_4 at pH = 6, respectively, at several current densities. The PMo_{12} specific capacities corresponded to 47.1, 46.9, 45.0, and 42.2 $mAh.g^{-1}$ under current densities of 0.1, 0.2, 0.5, and 1.0 $mA.cm^{-2}$, respectively. In addition to the lower dependence on current density, the specific capacity values were higher than the specific capacity values observed for previously investigated electrodes consisting of PMo_{12} adsorbed on carbon black [9]. This indicated that the support material increased the electrode charge storage capacity, mainly for the highest current densities.

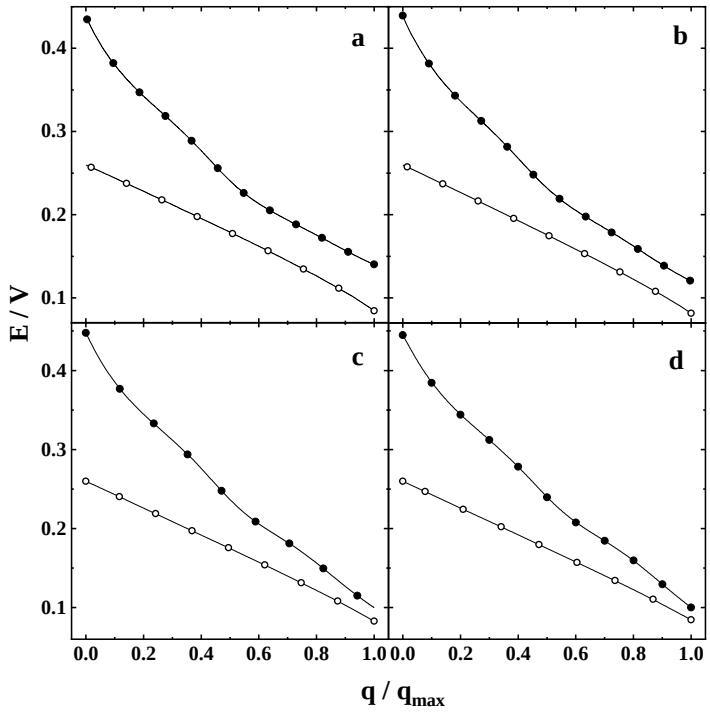

Figure 6 – PMo_{12}/RGO electrode (—●—) reduction (in 20 mM K_2SO_4 at pH = 2) and (—○—) oxidation (in 500 mM K_2SO_4 at pH = 6) curves. q_{max} = 42.4, 42.2, 40.5, and 38.0 mC at 0.1, 0.2, 0.5, and 1.0 $mA.cm^{-2}$, respectively. PMo_{12} mass = 0.25 mg.

Given that protons were removed from the concentrated medium (pH = 2) to the diluted medium (pH = 6), the areas between the curves, multiplied by the Faraday constant, corresponded to the values of energy harvested per mol of adsorbed protons for the several applied current densities. Meanwhile, the values of these areas divided by time (without counting the time related to solution replacement and neutralization) gave us the power density per mol of adsorbed protons (P). Figure 7 shows the values of harvested energy and power density per mol of adsorbed protons. While the harvested energy associated with the proton adsorption/desorption reaction in PMo_{12} sites did not vary significantly, the power density increased significantly as a function of the current density. This behavior was due to the small variations in overpotential, even for the highest current densities, indicating fast charge transfer, as will be shown below.

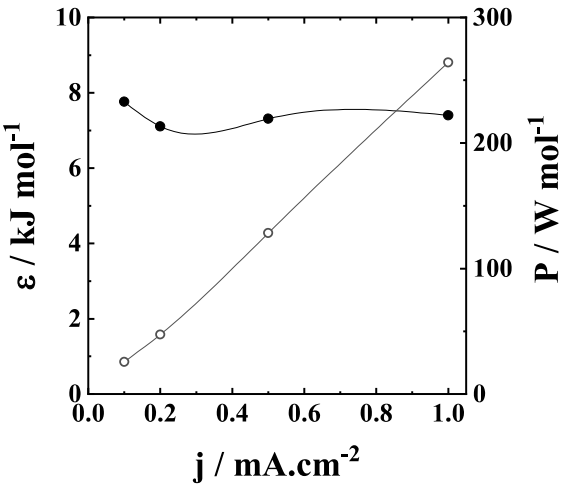

Figure 7 – (—●—) Harvested energy and (—○—) power density per mol of adsorbed protons as a function of the current density.

To define the slowest electrochemical step(s), which account(s) for the highest contribution(s) to the overpotentials and, consequently, to the highest energy dissipation (heat), we conducted electrochemical impedance spectroscopy for proton adsorption/desorption in the PMo_{12}/RGO electrode. Figure 8 shows the Nyquist impedance diagrams for the experimental and theoretical data associated with the redox process in the PMo_{12}/RGO electrode in (a) 20 mM K_2SO_4 at pH = 2 and (b) 500 mM K_2SO_4 at pH = 6.0, respectively. The semicircle at high frequencies referred to the charge transfer related to proton adsorption/desorption and electrical double-layer charging. The capacitive behavior at low frequencies was related to the coverage of electroactive sites due to proton adsorption. The impedance data observed at intermediate frequencies, between the semicircle and the capacitive behavior, was associated with the transport of the electrolyte solution ions into the pores and of electrons in the solid phase of the electrode [28]. Table 2 lists the parameters obtained from the fittings (by using Equation 16, 21, and 22).

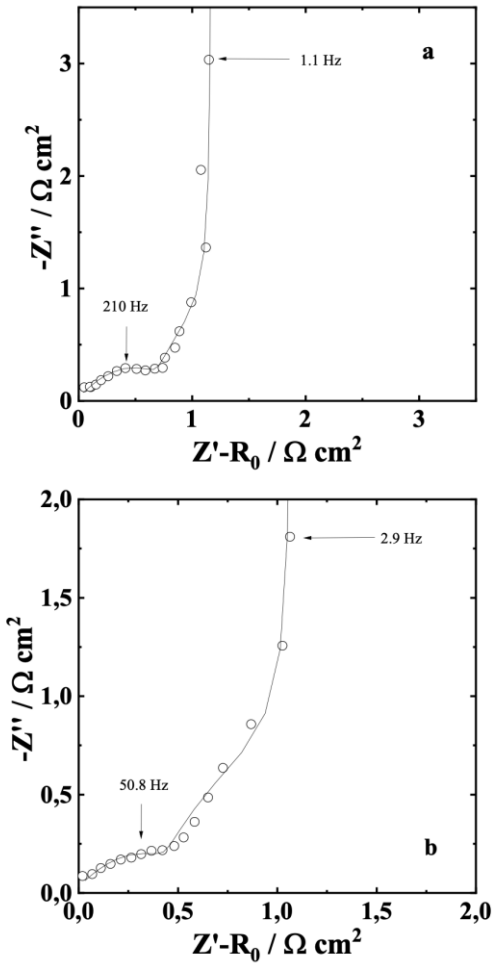

Figure 8 - Nyquist impedance diagrams for the (○) experimental and (—) theoretical data associated with proton adsorption/desorption in PMo_{12}/RGO in (a) 20 mM K_2SO_4 (pH = 2) at 0.25 V and (b) 500 mM K_2SO_4 (pH = 6) at 0.15 V.

Table 2 - Parameters determined from fitting of the impedance data for proton adsorption/desorption in the PMo_{12}/RGO electrode at pH = 2 (in 20 mM K_2SO_4) and at pH = 6 (in 500 mM K_2SO_4).

pH	E /V	R_{ct} /Ω	k_1 /molcm^{-2}s^{-1}	k_1' /molcm^{-2}s^{-1}	C_{dl} /mF	κ /mS.cm^{-1}	σ /mS.cm^{-1}	a	Γ/(k_1+k_1') /ms	θ	ΓF /mC.cm^{-2}	L /μm	β
2.0	0.25	0.55	1.4 x 10^{-5}	4.7 x 10^{-7}	3.0	0.1	100	8000	8.5	0.96	11.4	3.1	1
6.0	0.15	0.25	3.1 x 10^{-5}	1.1 x 10^{-6}	4.0	0.1	100	8000	4.0	0.96	12.0	3.1	1

On the basis of the charge transfer resistance and rate constant values determined for proton adsorption/desorption in PMo_{12}/RGO, we observed lower irreversibility as compared to other materials containing PMo_{12} that have been previously used in these electrochemical systems, but the injected charge was higher in the present study [13,24]. Thus, low overpotentials were expected, as shown above, which enabled more efficient energy harvesting due to low heat dissipation. This performance should be associated with dispersion of the PMo_{12} clusters on large surface area support material, which allowed many electroactive sites that can be easily accessed by protons to be anchored, changing energy harvesting very little and significantly enhancing power as a function of the current density, as shown above.

The electronic resistance of the solid material and the ionic resistance of the electrolyte solution in the electrode material pores were not high enough to contribute to heat dissipation significantly, as shown in the Nyquist diagrams in Figure 8. Thus, the electrolyte solution must have filled the electrode material pores given that the PMo_{12}/RGO composite is mesoporous [14], and protons from the electrolyte solution were able to access PMo_{12} clusters inside and outside the pores easily.

In the same way that we carried out electrochemical experiments for the PMo_{12}/RGO electrode at different pH values to verify the pH range in which the electrode is stable, we performed electrochemical experiments for the CuHCF electrode. Figures 9 a-g display cyclic voltammograms for the CuHCF electrode (the current density is normalized by the maximum current density of the first voltammogram) in 20 mM K_2SO_4 solution at several pH values. We found that the CuHCF electrode is chemically unstable at pH = 1 and ≥ 10 because CN^- is released from the CuHCF structure [39]. On the basis of these data and of the data related to the PMo_{12}/RGO electrode, the proposed electrochemical system should operate at pH ranging from 2 to 6, as mentioned previously.

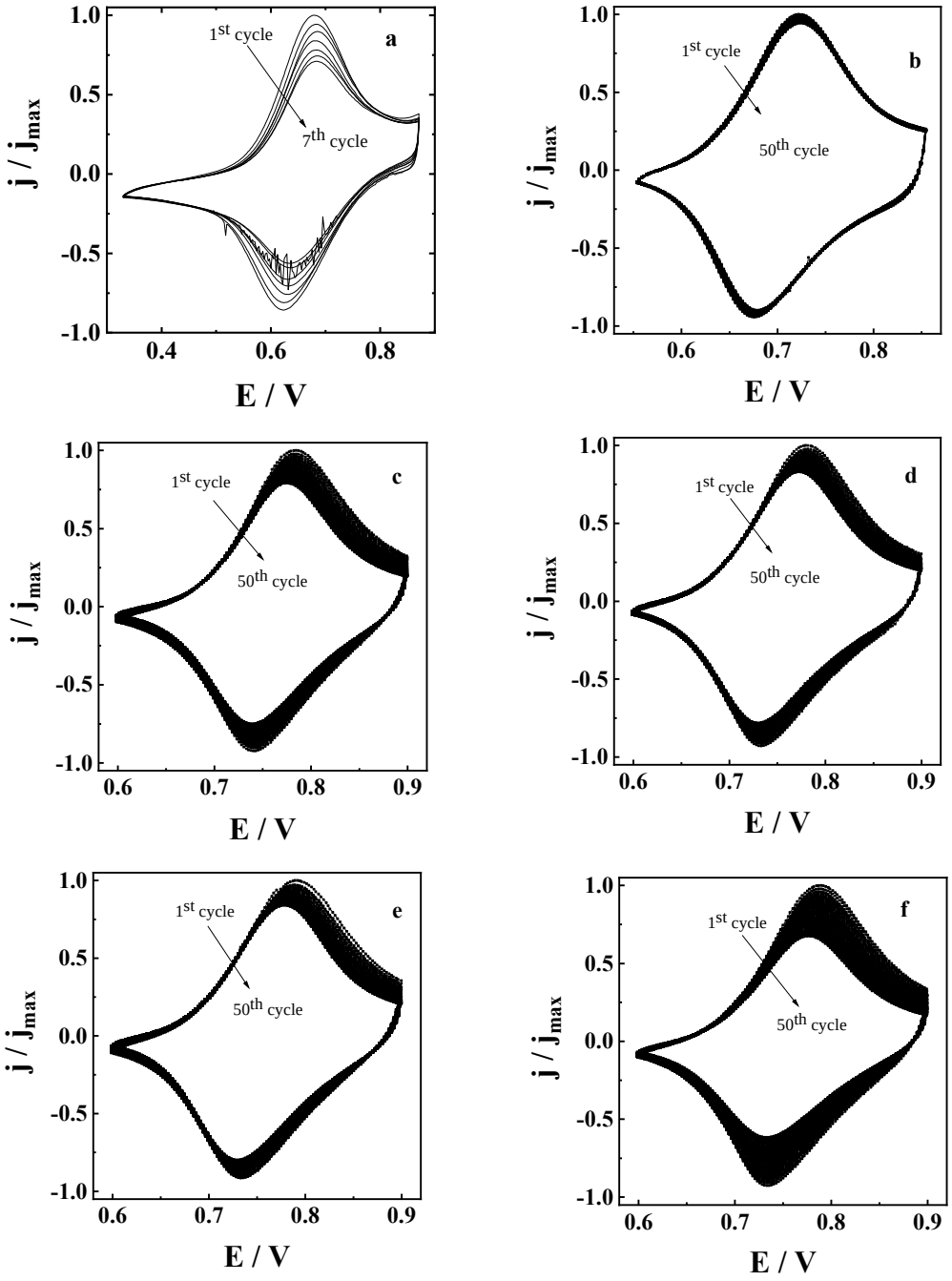
a
1st cycle
7th cycle
b
1st cycle
50th cycle
c
1st cycle
50th cycle
d
1st cycle
50th cycle
e
1st cycle
50th cycle
f
1st cycle
50th cycle
j / jmax
E / V

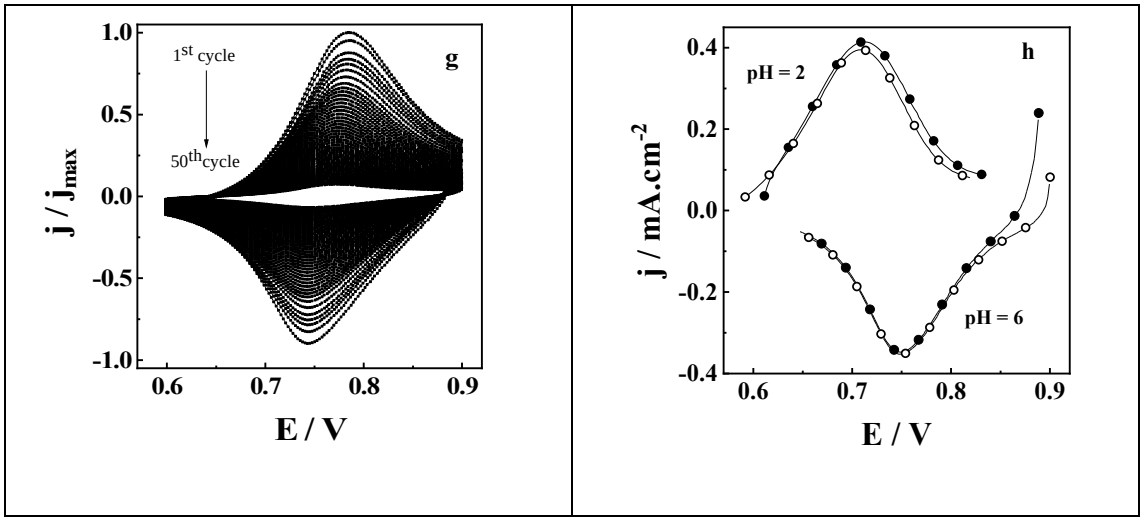

Figure 9 – Cyclic voltammograms recorded for the CuHCF electrode: in 20 mmol.L^{-1} K_2SO_4 at a) pH = 1 (j_{max} = 0.26 mA.cm^{-2}); in 500 mmol.L^{-1} K_2SO_4 at b) pH = 2 (j_{max} = 0.25 mA.cm^{-2}), c) pH = 7 (j_{max} = 0.25 mA.cm^{-2}), d) pH = 8 (j_{max} = 0.27 mA.cm^{-2}), e) pH = 9 (j_{max} = 0.25 mA.cm^{-2}), f) pH = 10 (j_{max} = 0.25 mA.cm^{-2}), and g) pH = 11 (j_{max} = 0.26 mA.cm^{-2}). The arrow indicates the direction from the first to the last voltammogram. h) (—○—) linear sweep toward more negative potentials in 500 mM K_2SO_4 at pH = 6, followed by linear sweep toward more positive potentials at pH = 2 without K_2SO_4 in solution; (—●—) linear sweep toward more negative potentials in 500 mM K_2SO_4 at pH = 6, followed by linear sweep toward more positive potentials at pH = 2 in 20 mM K_2SO_4 in solution. The pH solution is shown in Figures. ν = 1 mV.s^{-1}.

Figure 9h shows linear sweeps we conducted to investigate how K_2SO_4 in solution affected energy harvesting when its concentration increased from 0 to 20 mM in step I, for the experimental conditions used in this work. We performed a linear sweep toward more negative potentials in 500 mM K_2SO_4 solution at pH = 6. When the circuit was open, the potential was 0.660 V. After that, we exchanged the solution for another at pH = 2 without K_2SO_4, and the open circuit potential shifted to 0.598 V. We performed a linear sweep toward more positive potentials to compare it with the result obtained during potassium ion deintercalation from the CuHCF electrode in 20 mM K_2SO_4 at pH = 2.

Thus, again we accomplished another linear sweep toward more negative potentials in 500 mM K_2SO_4 solution at pH = 6 to intercalate potassium ions in the CuHCF electrode. Subsequently, we replaced the solution with another 20 mM K_2SO_4 solution at pH = 2 (the open circuit potential shifted from 0.661 to 0.602 V). Finally, we performed a linear sweep toward more positive potentials. We observed that the open circuit potential and the potential profile of the linear sweep were close to those observed for the solution without K_2SO_4. This indicated that energy harvesting did not vary significantly when the concentration of this salt in the solution varied from 0 to 20 mM. As the addition of K_2SO_4 in step I reduced the resistance of the solution at pH = 2 (38.9 Ω and 21.4 Ω for the solution without salt and in 20 mM K_2SO_4, respectively, as verified by impedance measurements), electrodes with large geometric area (larger than the area used in this work) should undergo a smaller decrease in energy harvesting due to ohmic drop under higher electrical current.

Figure 10 shows the equilibrium potential as a function of the charge normalized by the maximum charge, associated with potassium ion intercalation/deintercalation in/from the CuHCF electrode, in 20 mM K_2SO_4 at pH = 2.0 and in 500 mM K_2SO_4 at pH = 6.0. In this case, the maximum energy harvested per mol of intercalated potassium ion corresponded to 6.89 kJ mol^{-1} and was associated with the contribution of the mixing free energy related to the alkali metal ion concentration difference of the electrolyte solutions.

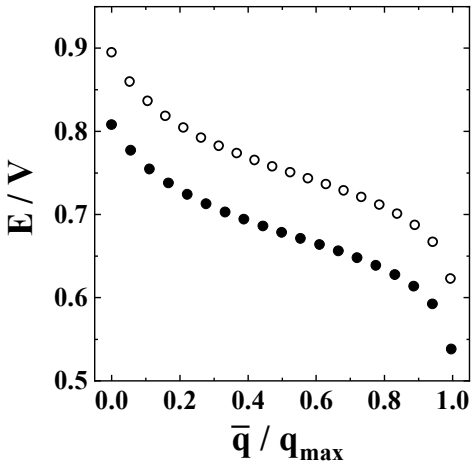

Figure 10 – Measured CuHCF electrode equilibrium potential as a function of normalized charge in (●) 20 mM K_2SO_4 at pH = 2 and (○) 500 mM K_2SO_4 at pH = 6. q_{max} = 41.3 mC.

We also recorded electro-oxidation curves in 20 mM K_2SO_4 at pH = 2 and electro-reduction curves in 500 mM K_2SO_4 at pH = 6 for the CuHCF electrode (Figure 11). The specific capacities corresponded to 52.2, 49.4, 46.7, and 44.0 $mAh.g^{-1}$ under current densities of 0.1, 0.2, 0.5, and 1.0 $mA.cm^{-2}$, respectively. These specific capacity values were close to the specific capacity values observed for potassium ion intercalation/deintercalation in/from CuHCF electrodes [36]. The CuHCF specific capacity resembles the specific capacity of nickel hexacyanoferrate (NiHCF), which we also used as positive electrode for energy harvesting in a similar electrochemical system [9]. However, the decrease in specific capacity as a function of the current density was lower for the CuHCF electrode, which indicated better performance at the highest current densities. On the other hand, this specific capacity variation under the applied current density range was higher than the variation related to proton adsorption/desorption in the PMo_{12}/RGO electrode, which was related to higher overpotential for the potassium ion intercalation/deintercalation reaction in/from the CuHCF electrode.

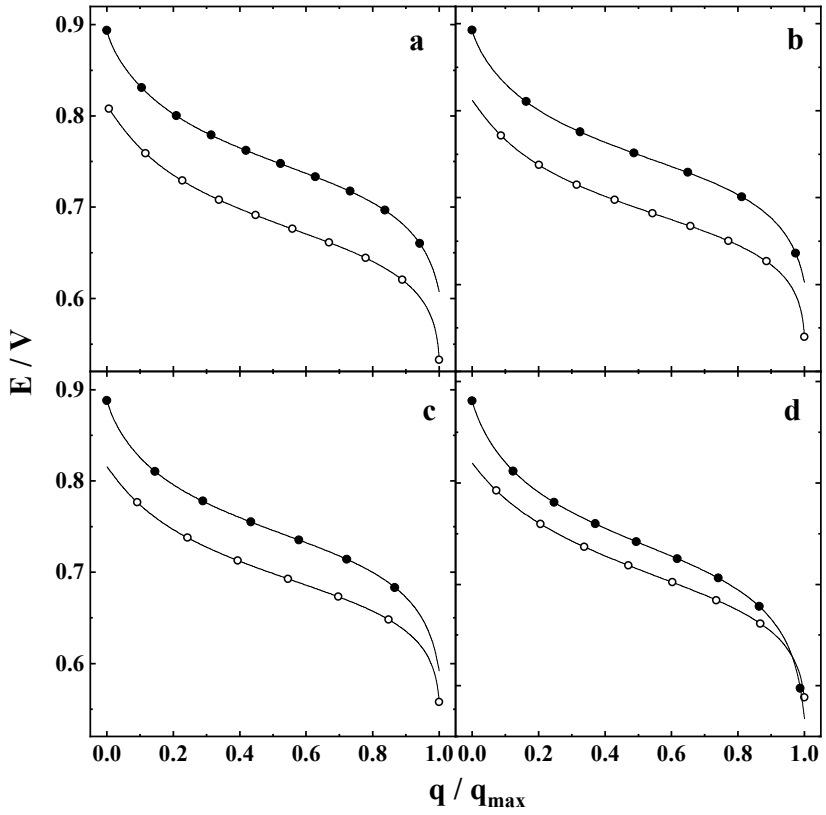

Figure 11 - (a) (—○—) Oxidation (in 20 mM K_2SO_4 at pH = 2) and (—●—) reduction (in 500 mM K_2SO_4 at pH = 6) curves of the CuHCF electrode, associated with potassium ion deintercalation and intercalation, respectively. q_{max} = 47.0, 44.5, 42.1, and 39.6 mC at 0.1, 0.2, 0.5, and 1.0 $mA.cm^{-2}$, respectively. CuHCF mass = 0.25 mg.

The area between the curves shown in Figure 11, multiplied by the Faraday constant, corresponded to the energy harvested per mol of intercalated potassium ion, which was also associated with the mixture free energy. In fact, after the electrochemical cycle, the potassium ions removed from the concentrated saline solution were added to the diluted saline solution. On the basis of these data, the harvested energy and power density as a function of the current density are shown in Figure 12. Although the specific capacity did not vary significantly as a function of the current density, the energy decreased considerably for higher current densities, unlike the energy harvested from proton adsorption/desorption in PMo_{12}/RGO. This difference in behavior was due to the higher overpotentials observed in the electrochemical reaction involved in the CuHCF

electrode as compared to the electrochemical reaction involved in the PMo_{12}/RGO electrode during the electrochemical cycles, which also explained the curve profile for the power density as a function of current density, where the values deviated significantly from linearity.

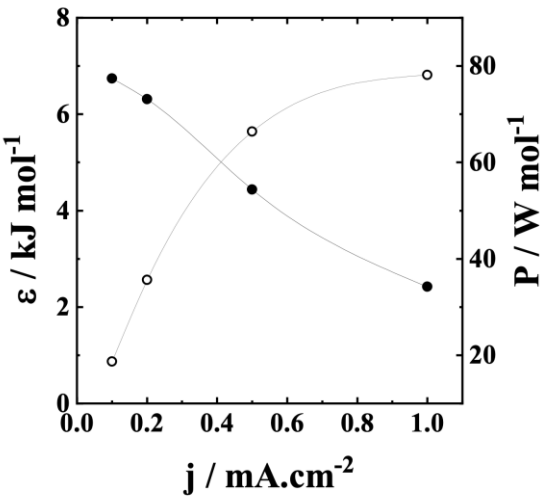

Figure 12 – (—●—) Harvested energy and (—○—) power density per mol of potassium ions intercalated in the CuHCF electrode as a function of the current density in 20 mM K_2SO_4 at pH = 2 and in 500 mM K_2SO_4 at pH = 6.

To confirm that potassium ions participate in the charge compensation mechanism associated with the faradaic reaction in the CuHCF electrode, cyclic voltammograms for the CuHCF electrode are illustrated in Figure 13a (pH = 2; several K_2SO_4 solution concentrations at 1 mV s^{-1}). The peak potentials changed to more positive values when the potassium ion concentration increased, indicating that these ions intercalated/deintercalated in/from the CuHCF electrode (given that the equilibrium potential is a function of the activity of these ions in the electrolyte solution) at least at the lowest pH limit proposed for energy harvesting in this work (pH = 2). On the other hand, the voltammetric peaks did not shift when the K_2SO_4 concentration was kept constant (20 mM) and the pH changed from 2.0 to 6.0 (Figure 13b), which suggested

minimum or no proton intercalation/deintercalation in this pH range, as mentioned in the literature [18,25]. However, protons could have greater participation in the charge compensation process at lower pH values. Thus, we also performed cyclic voltammetry experiments with and without K_2SO_4 at pH = 2 (Figure 14a). The voltammetric profiles were different, and the current density obtained in the absence of K_2SO_4 was much lower than the current density recorded in the presence of potassium ions, which suggested that protons were intercalated/deintercalated in/from the CuHCF electrode in the absence of potassium ions in the electrolyte solution. However, there was a significant preference for potassium ion intercalation over protons even for higher proton concentrations, as shown in Figure 14b, where cyclic voltammograms in 10 mM K_2SO_4 are displayed for various H_2SO_4 concentrations. Observe that the voltammetric profiles and peak potentials were close to those shown in Figures 13a and 13b, suggesting that most of the alkali metal ion participated in the charge compensation process. However, in contrast to Figure 13b, the peak potentials shifted to more negative potentials, and the voltametric profile changed slightly at high proton concentration; e.g., at 30 mM H_2SO_4.

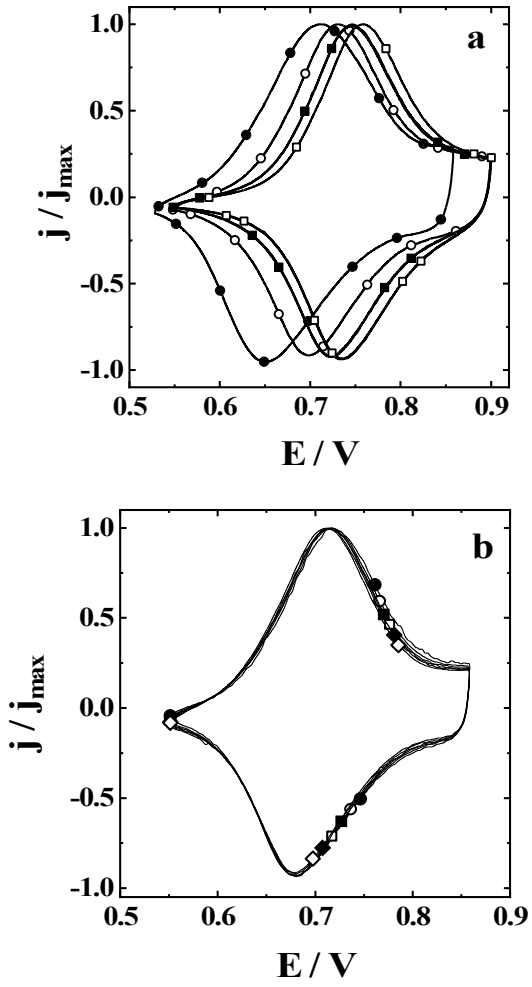

Figure 13 – (a) Cyclic voltammetry of the CuHCF electrode in electrolyte solution at pH = 2 and several K_2SO_4 concentrations: (—●—) 20 mM K_2SO_4, j_{max} = 0.26 mA.cm^{-2}; (—○—) 65 mM K_2SO_4, j_{max} = 0.26 mA.cm^{-2}; (—■—) 150 mM K_2SO_4, j_{max} = 0.25 mA.cm^{-2}; (—□—) 500 mM K_2SO_4, j_{max} = 0.25 mA.cm^{-2}. CuHCF mass = 0.25 mg. (b) Cyclic voltammetry of the CuHCF electrode in 50mM K_2SO_4 electrolyte solution at several pH values: (—●—) pH=2.00; (—○—) pH=2.25; (—■—) pH=2.50; (—□—) pH=2.75; (—◆—) pH=3.00; (—◇—) pH=4.00. j_{max} = 0.26 mA.cm^{-2}. ν = 1mV⁄s. CuHCF mass = 0.25 mg.

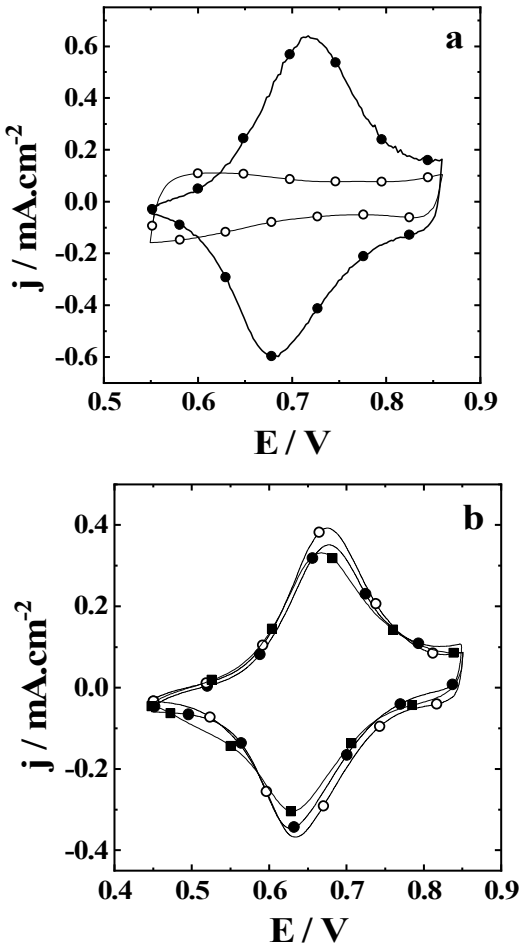

Figure 14 – Cyclic voltammetry of the CuHCF electrode a) in H_2SO_4 solution at pH = 2.0 with (—●—) 50 mmol.L^{-1} K_2SO_4 and (—○—) without K_2SO_4. ν = 1 mV.s^{-1}; (b) in 10 mmol.L^{-1} K_2SO_4 solution at several H_2SO_4 concentration values: (—●—) 7.5 mmol.L^{-1} H_2SO_4, (—○—) 15 mmol.L^{-1} H_2SO_4, and (—■—) 30 mmol.L^{-1} H_2SO_4. ν = 1 mV.s^{-1}.

These results are important for the full electrochemical cell proposed here because, as the electrochemical processes only involve proton participation in the PMo_{12}/RGO electrode (Equation 1) [37], minimum or no proton participation in the charge compensation process during CuHCF electrooxidation/electroreduction guarantees the highest energy harvesting after the cycle. Otherwise, the electric potential of the positive electrode (CuHCF) would tend to increase in low pH solutions (which would increase the electrical energy involved in the non-spontaneous process) and to decrease at higher pH values (which would decrease the electrical energy involved in the

spontaneous process). This would result in lower energy harvesting values (in the case potassium ions do not participate, energy harvesting would be impossible due to heat dissipation during the electrochemical cycle).

Figure 15 displays the Nyquist impedance diagrams for the experimental and theoretical data associated with potassium ion intercalation/deintercalation in/from the CuHCF electrode in (a) 20 mM K_2SO_4 at pH = 2.0 and (b) 500 mM K_2SO_4 at pH = 6.0, respectively. We noticed charge transfer resistance and electrical double-layer charging at high frequencies. Ion transport from the electrolyte solution in the electrode pores, together with electron transport in the solid phase was evident from the shape of the 45° slope at high and intermediate frequencies. Meanwhile, we verified potassium ion-electron pair semi-infinite diffusion at intermediate frequencies, which was also evident from the shape of the 45° slope, and its finite diffusion into the CuHCF particles at low frequencies, which corresponded to capacitive behavior.

Table 3 summarizes the parameters of Equations 20-22 used in the fittings. Although the presence of copper ions in the hexacyanometalate structure increased the potassium ion diffusion rate [18] (the diffusion coefficient values for potassium ions into the CuHCF were one order higher than those determined for Prussian Blue [40] and in the same order of magnitude as sodium ion intercalation/deintercalation [41]), the diffusion and charge transfer resistance values revealed that deintercalation/intercalation of this alkali metal ion from/in the CuHCF electrode in diluted/concentrated medium limited the rate of the full cell electrochemical steps II/IV. This observation was also supported by the frequencies associated with the finite diffusion, which were lower (higher average time) than those related to proton adsorption on the PMo_{12}/RGO electrode. These impedance data explained the profile of the curves in Figure 12, which demonstrated decreased energy harvesting and higher dependence of power density as a function of the current density than the curves in Figure 7.

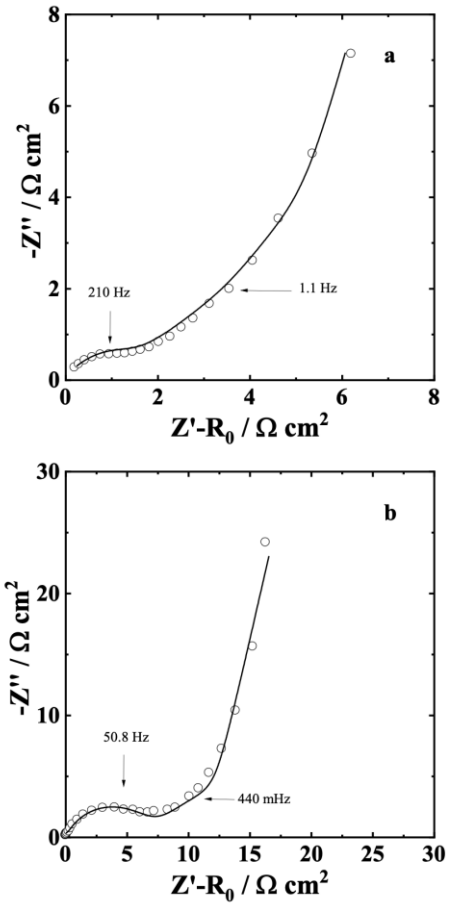

Figure 15 - Nyquist impedance diagrams for the (○) experimental and (—) theoretical data associated with potassium ion intercalation/deintercalation in/from CuHCF in (a) 20 mM K_2SO_4 (pH = 2) at 0.70 V and (b) 500 mM K_2SO_4 (pH = 6) at 0.75 V.

Table 3 - Parameters determined from fitting of the impedance data for potassium ion intercalation/deintercalation in/from the CuHCF electrode at pH = 2 (in 20 mM K_2SO_4) and at pH = 6 (in 500 mM K_2SO_4).

pH	E /V	R_{ct} /Ω	k /molcm^{-2}s^{-1}	C_{dl} /mF	κ /mS.cm^{-1}	σ /μS.cm^{-1}	a	D /cm^2.s^{-1}	l /nm	L /μm	C_L /mF	β	γ
2.0	0.70	0.4	1.4 x 10^{-6}	3.0	0.1	20	8000	1.3 x 10^{-9}	50	0.2	350	1.0	0.86
6.0	0.75	11.5	0.5 x 10^{-7}	4.0	0.1	100	9000	0.6 x 10^{-9}	50	0.2	170	0.8	0.86

We predicted full cell results on the basis of the data shown above (half-cell measurements). Figure 16a shows the curves associated with the equilibrium potential

difference in 20 mM K_2SO_4 at pH = 2.0 and in 500 mM K_2SO_4 at pH = 6.0 for the full cell, from which we determined the maximum harvested energy (14.5 kJ mol^{-1}). Figures 16b-e display examples of the full cell potential difference as a function of the charge normalized by the maximum charge at several current densities. From these curves, we determined the harvested energy and power density (Figure 16f) per mol of proton adsorbed on PMo_{12}/RGO (or per mol of potassium ion intercalated into CuHCF) for several current densities. Note that the power density profile for the full cell resembled the profile shown in Figure 7 given that the power density associated with proton adsorption/desorption in PMo_{12}/RGO was much greater than the power density associated with potassium ion intercalation/deintercalation in/from CuHCF. Another important aspect to consider when evaluating the feasibility of applying energy conversion devices is their cyclability. Thus, Figure 16g displays the harvested energy and power density from the first to the twentieth cycle, where we can observe a small variation around 13.5 kJ mol^{-1} and 43 W mol^{-1} at 0.1 mA cm^2.

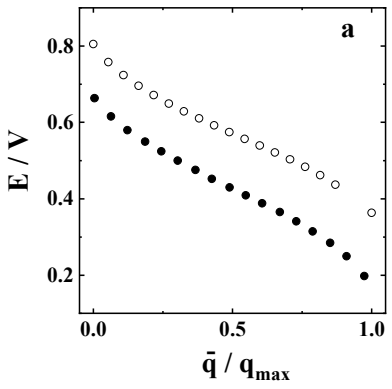

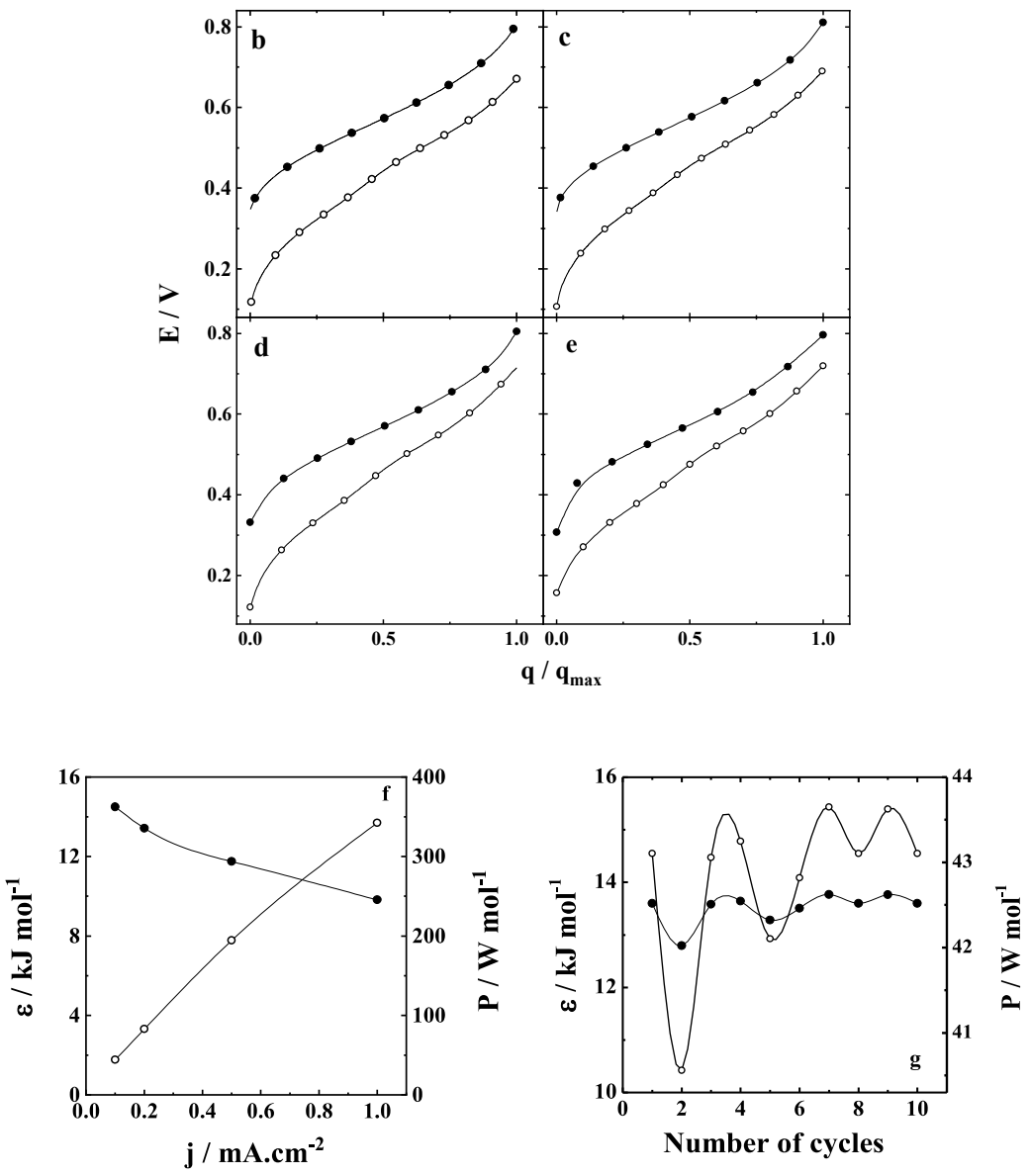

Figure 16 - (a) Predicted full cell potential difference at equilibrium in 20 mM K_2SO_4 at pH = 2.0 (—●—) and in 500 mM K_2SO_4 at pH = 6.0 (—○—), and as a function of the charge normalized for the several applied current densities: (b) j = 0.1 mA.cm^{-2} (q_{max} = 42.4 mC), (c) j = 0.2 mA.cm^{-2} (q_{max} = 42.4 mC), (d) j = 0.5 mA.cm^{-2} (q_{max} = 40.5 mC), and (e) j = 1.0 mA.cm^{-2} (q_{max} = 38.0 mC). (f) Harvested energy (—●—) and power density (—○—) per mol of adsorbed proton for several current densities. (g) Predicted energy harvesting and power density as a function of the number of cycles at 0.1 mA cm^2.

On the basis of these data, the harvested energy was comparable to the harvested energy associated with other electrochemical systems that harvest energy from the difference in ion concentrations, like CAPMIX and Mixing Entropy Batteries [1,5,7,42-47]. However, the harvested energy was higher than the energy harvested from similar systems; e.g., PMo_{12} adsorbed on carbon black and nickel hexacyanoferrate (5.0 kJ mol^{-1} at 0.2 mA cm^{-2}) [9]. Table 4 shows the harvested energy and power density values of full cells, normalized by the number of ions participating in the electrochemical reactions. More information about materials and their energy storage capacities due to variation in ion concentrations can be seen in reference [8].

Table 4 – Composition, energy harvesting, and power density for full electrochemical cells under constant current density.

Ref.	Positive Electrode	Negative Electrode	Energy Harvesting/ $kJ.cm^{-2}.mol^{-1}$	Power Density/W. $cm^{-2}.mol^{-1}$	Current Density/mA.cm^{-2}
[8]	$FePO_4$	Ag	12.3	4.43	0.25
[5]	$Na_2Mn_5O_{10}$	Ag	9.33	3.37	0.25
[9]	$KNi[Fe(CN)_6]$	PMo_{12}/CB	5.00	47.20	0.20
[42]	$Na_4Mn_9O_{18}$	Ag	4.82	0.89	1.00
[43]	MnO_2	Pb	9.17	25.32	0.20
[44]	$KCu[Fe(CN)_6]$	BiOCl	9.65	69.95	0.20
[45]	$Na_{0.44}MnO_2$	Ag	0.64	1.78	1.00
[46]	PTSA	PEI-EN	2.12	21.22	1.00
[47]	EDA	PAA-PMA	5.64	31.33	0.5
	$KCu[Fe(CN)_6]$**	PMo_{12}/RGO**	9.8	345.40	1.00

*CB ≡ carbon black; PAH ≡ poly(allylamine hydrochloride); PSS ≡ poly(styrene sulfonate); PEDOT ≡ poly(3,4-ethylenedioxythiophene); PTSA ≡ p-toluensulfonic acid; PEI-EN ≡polyethylene branched with ethylene diamine; EDA ≡ ethylenediamine; PAA ≡ poly(acrylic acid); PMA ≡ poly(methacrylic acid).
**data from this work.

CONCLUSIONS

This work has investigated electrodes consisting of PMo_{12}/RGO and CuHCF for proton adsorption/desorption and potassium ion intercalation/deintercalation, respectively, which can be used to harvest electrical energy associated with changes in the concentration of these ionic species in the course dilution/neutralization processes. On the basis of the measurements along time, we observed low practical proton adsorption/desorption irreversibility on PMo_{12} clusters anchored on reduced graphene

oxide, which provides a large surface area support material. This low practical irreversibility corroborated by the rate constant values, determined from the measurements and kinetic model in the frequency domain, ensured low overpotentials at the applied current densities and allowed higher energy conversion. On the basis of the kinetic model in the frequency domain, we also determined the kinetic parameters for potassium ion intercalation/deintercalation in/from the CuHCF electrode. Copper ions inserted in the hexacyanometalate structure enabled higher ionic mobility as compared to the electrode formed from Prussian Blue, enhancing the energy harvested by the full cell. The resulting energy harvesting and power density corresponded to values around 13 kJ and 40 W per mol of adsorbed proton for the first twenty cycles at 0.1 mA cm^2. Although the use of these electrochemical systems is still far from being a reality (because no wastewater was used and the electric charge per unit volume of acid solution was still low for practical applications), this work demonstrates progress in the implementation of this idea for wastewater treatment given that electrodes with a higher amount of electroactive materials, as compared to the previously investigated materials, were used for energy harvesting during the dilution/neutralization process.

CONFLICTS OF INTEREST

There are no conflicts of interest to declare.

ACKNOWLEDGMENTS

We are grateful to FAPESP (Project 2018/07906-9 and 2021/12735-1) and CNPq (Project 140499/2021-0) for financial support.

REFERENCES

[1] F. Galleguillos, L. Cáceres, L. Maxwell, A. Soliz, Electrochemical Ion Pumping Device for Blue Energy Recovery: Mixing Entropy Battery, Appl. Sci. 10 (2020) 5537-5559.
[2] R. E. Pattle, Production of Electric Power by Mixing Fresh and Salt Water in the Hydroelectric Pile. Nature 174 (1954) 660.
[3] R. S. Norman, Water salination: a source of energy, Science 186 (1974) 350–352.
[4] S. Loeb, A method and apparatus for generating power utilizing pressure-retarded-osmosis, US Patent 3906250 (1975).
[5] F. La Mantia, M. Pasta, H. D. Deshazer, B. E. Logan, Y. Cui, Batteries for Efficient Energy Extraction from a Water Salinity Difference, Nano Lett. 11 (2011) 1810.
[6] J. Lee, H. Yoon, J. Lee, T. Kim, J. Yoon, Extraction of Salinity-Gradient Energy by a Hybrid Capacitive-Mixing System, ChemSuSChem 10 (2017) 1600-1606.
[7] D. Brogioli, Extracting Renewable Energy from a Salinity Difference Using a Capacitor, Phys. Rev. Lett. 103 (2009) 58501.
[8] F. Galleguillos, L. Cáceres, L. Maxwell, Á. Soliz, Electrochemical Ion Pumping Device for Blue Energy Recovery: Mixing Entropy Battery, Appl. Sci. 10 (2020) 5537-5550.
[9] G. Lima, D. P. Dubal, D. Rueda-García, P. Gómez-Romero, F. Huguenin, Energy harvesting from neutralization reactions with saline feedback, Electrochim. Acta 275 (2018) 145-154.
[10] W. G. Morais, G. Lima, W. J. A. S. Gomes, F. Huguenin, Electrochemical Systems for Renewable Energy Conversion from Salinity and Proton Gradients. J. Braz. Chem. Soc. 29 (2018) 934-947.
[11] W. G. Morais, W. J. A. S. Gomes, F. Huguenin, Neutralization Pseudocapacitors: An Acid-Base Machine, J. Phys. Chem. C 120 (2016) 17872-17877.
[12] J. Suárez-Guevara, V. Ruiz, P. Gómez-Romero, Stable graphene–polyoxometalate nanomaterials for application in hybrid supercapacitors, Phys. Chem. Chem. Phys. 16 (2014) 20411-20414.
[13] T. Facci, W. J. A. S. Gomes, B. Bravin, D. M. Araújo, F. Huguenin, Proton electroinsertion in self-assembled materials for neutralization pseudocapacitors, Langmuir 30 (2014) 426.
[14] D. P. Dubal, J. Suarez-Guevara, D. Tonti, E. Enciso, P. Gomez-Romero, A high voltage solid state symmetric supercapacitor based on graphene–polyoxometalate hybrid electrodes with a hydroquinone doped hybrid gel-electrolyte, J. Mater. Chem. A 3 (2015) 23483-23492.
[15] A. Razaq, F. Bibi, X. Zheng, R. Papadakis, S. H. M. Jafri, H. Li, Review on Graphene-, Graphene Oxide-, Reduced Graphene Oxide-Based Flexible Composites: From Fabrication to Applications, Materials 15 (2022) 1012.
[16] J. Tessonnier, S. Goubert-Renaudin, S. Alia, Y. Yan, M. Barteau, Structure, Stability, and Electronic Interactions of Polyoxometalates on Functionalized Graphene Sheets, Langmuir 29 (2013) 393-402.
[17] D. P. Dubal, D. Rueda-Garcia, C. Marchante, R. Benages, P. Gomez-Romero, Hybrid Graphene-Polyoxometalates Nanofluids as Liquid Electrodes for Dual Energy Storage in Novel Flow Cells, Chem. Rec. 18 (2018) 1-10.
[18] K. Hurlbutt, S. Wheeler, I. Capone, M. Pasta, Prussian Blue Analogs as Battery Materials, Joule 2 (2017) 1950–1960.
[19] M. Pasta, C. D. Wessells, N. Liu, J. Nelson, M. T. McDowell, R. A Huggins, M. F. Toney, Y. Cui, Full open-framework batteries for stationary energy storage, Nat. Commun. 5 (2014) 3007.

[20] V. Ganesh, D. L. Maheswari, S. Berchmans, Electrochemical behaviour of metal hexacyanoferrate converted to metal hydroxide films immobilized on indium tin oxide electrodes—Catalytic ability towards alcohol oxidation in alkaline medium, Electrochim. Acta 56 (2011) 1197.
[21] G. Lima, F. Huguenin, Transference function for electro-insertion reactions in blue energy devices and acid-base machines, Electrochim. Acta 305 (2019) 312-321.
[22] C. D. Wessells, M. T. McDowell, S. V. Peddada, M. Pasta, R. A. Huggins, Y. Cui, Tunable Reaction Potentials in Open Framework Nanoparticle Battery Electrodes for Grid-Scale Energy Storage, ACS Nano 6 (2012) 1688-1694.
[23] W. J. A. S. Gomes, C. de Oliveira, F. Huguenin, Energy Harvesting by Nickel Prussian Blue Analogue Electrode in Neutralization and Mixing Entropy Batteries, Langmuir 31 (2015) 8710-8717.
[24] G. Lima, W. G. Morais, W. J. A. S. Gomes, F. Huguenin, Acid–base machines: electrical work from neutralization reactions, Phys. Chem. Chem. Phys. 19 (2017) 31202-31215.
[25] C. D. Wessells, S. V. Peddada, M. T. McDowell, R. A. Huggins, Y. Cui. The effect of insertion species on nanostructured open framework hexacyanoferrate battery electrodes. J. Electrochem. Soc. 159 (2012) A98-A103.
[26] M. E. Orazem and B. Tribollet, Electrochemical impedance spectroscopy, Wiley, Hoboken, NJ, 2008.
[27] C. Ho, I. D. Raistrick and R. A. Huggins, Application of A-C Techniques to the Study of Lithium Diffusion in Tungsten Trioxide Thin Films, J. Electrochem. Soc., 127 (1980) 343–350.
[28] U. Tröltzsch, O. Kanoun, Generalization of transmission line models for deriving the impedance of diffusion and porous media, Electrochimica Acta 75 (2012) 347.
[29] A. Seidell, W. F. Linke, Solubilities of Inorganic and Organic Compounds. 3rd edition, Van Nostrand, New York, 1952.
[30] H. E. Wirth, Activity coefficients in H_2SO_4 and H_2SO_4-Na_2SO_4 mixtures, Electrochim. Acta 16 (1971) 1345-1356.
[31] H. Aghaie, Z. Rezania, The solubility of potassium sulfate in thermodynamic view, J. Phys. Theor. Chem. 5 (2008) 115-118.
[32] W. Weppner, Electrode performance. In: P. Bruce (Ed.), Solid State Electrochemistry, Cambridge University Press, Cambridge, 1994, pp. 199-228.
[33] I. D. Raistrick, D. R. Franceschetti, J. R. Macdonald, Theory. In: E. Barsoukov, J. R. Macdonald (Eds.), Impedance Spectroscopy Theory, Experiment, and Applications, 2nd edition, John Wiley & Sons, New Jersey, 2005, pp. 27-128.
[34] Kim, H., Park, K.-Y., Hong, J. & Kang, K. All-graphene-battery: bridging the gap between supercapacitors and lithium ion batteries, Sci. Rep. 4 (2015) 5278.
[35] V. Ruiz, J. Suárez-Guevara, P. Gomez-Romero, Hybrid electrodes based on polyoxometalate–carbon materials for electrochemical supercapacitors, Electrochem. Commun. 24 (2012) 35-38.
[36] C. D. Wellells, R. A. Huggins, Y. Cui, Copper hexacyanoferrate battery electrodes with long cycle life and high power, Nat. Commun. 2 (2011) 550-554.
[37] M. Sadakane, E. Steckhan, Electrochemical Properties of Polyoxometalates as Electrocatalysts, Chem. Rev. 98 (1998), 219−237.
[38] Y. Yang, C. Brownell, N. Sadrieh, J. May, A. Del Grosso, D. Place, E. Leutzinger, E. Duffy, R. He, F. Houn, R. Lyon, P. Faustino, Quantitative measurement of cyanide released from Prussian Blue, Clin. Toxicol. 45 (2007) 776-781.

[39] M. Pasta, C. D. Wessells, N. Liu, J. Nelson, M. T. McDowell1, R. A. Huggins, M. F. Toney, Y. Cui, Full open-framework batteries for stationary energy storage, Nat. Commun. 5 (2014) 3007 – 3015.
[40] J. J. Garcia-Jarego, J. J. Navarro, A. F. Roig, H. Scholl, F. Vicente, Impedance analysis of Prussian Blue films deposited on ITO electrodes, Electrochim. Acta 40 (1995) 1113-1119.
[41] W. Wang, Y. Gang, Z. Hu, Z. Yan, W. Li, Y. Li, Q.-F. Gu, Z. Wang, S.-L. Chou, H.-K. Liu, S.-X. Dou, Reversible structural evolution of sodium-rich rhombohedral Prussian blue for sodium-ion batteries, Nat. Commun. 11 (2020) 980.
[42] M. Ye; M. Pasta; X. Xie, Y. Cui, S. Criddle, Performance of a Mixing Entropy Battery Alternately Flushed with Wastewater Effluent and Seawater for Recovery of Salinity-gradient Energy, Energy Environ. Sci. 7 (2014) 2295-2300.
[43] T. Kim, M. Rahimi, B. E. Logan, C. A. Gorski, Evaluating Battery-like Reactions to Harvest Energy from Salinity Differences using Ammonium Bicarbonate Salt Solutions, ChemSusChem 9 (2016) 981–988.
[44] G. Tan, X. Zhu, Polyelectrolyte-Coated Copper Hexacyanoferrate and Bismuth Oxychloride Electrodes for Efficient Salinity Gradient Energy Recovery in Capacitive Mixing, Energ Technol 8 (2019) 1900863
[45] M. Marino, L. Misuro, R. Ruffo, D. Brogioli, Electrode kinetic in the "capacitive mixing"and "battery mixing" techniques for energy production from salinity differences, Electrochim. Acta 176 (2015) 1065-1073.
[46] M. Marino, O. Kozynchenko, S. Tennison, D. Brogioli, Capacitive mixing with electrodes of the same kind for energy production from salinity differences, J. Phys.: Condens. Matter. 28 (2016) 114004-114013.
[47] A. Siekierka, K. Smolinska-Kempisty, M. Bryjak, Charge-doped electrodes for power production using the salinity gradient in CapMix, Desalination 495 (2020) 114670 – 114682.